Journal of Geophysical Research: Space Physics

RESEARCH ARTICLE
10.1029/2018JA025890

Key Points:
- When the radiation belt slot region is filled by electrons, their precipitation into the mesosphere increases and can be detected by radar
- Combined observations and models show electrons with energies >640 keV penetrate to ~55 km, potentially impacting atmospheric ozone
- Local time distribution of precipitation is similar to that of plasmaspheric hiss, suggesting hiss as the mechanism of precipitation

Correspondence to:
A. J. Kavanagh,
andkav@bas.ac.uk

Citation:
Kavanagh, A. J., Cobbett, N., & Kirsch, P. (2018). Radiation Belt slot region filling events: Sustained energetic precipitation into the mesosphere. *Journal of Geophysical Research: Space Physics*, *123*, 7999–8020. https://doi.org/10.1029/2018JA025890

Received 11 JUL 2018
Accepted 9 SEP 2018
Accepted article online 12 SEP 2018
Published online 28 SEP 2018

Radiation Belt Slot Region Filling Events: Sustained Energetic Precipitation Into the Mesosphere

Andrew J. Kavanagh[1,2], Neil Cobbett[1], and Peter Kirsch[1]

[1]British Antarctic Survey, Cambridge, UK, [2]Visiting Scientist at RAL Space, Rutherford Appleton Laboratory, Oxford, UK

Abstract Precipitation of energetic electrons to the atmosphere is both a loss mechanism for radiation belt particles and a means by which the geospace environment influences the Earth's atmosphere; thus, it is important to fully understand the extent of this precipitation. A set of polar orbiting satellites have been used to identify periods when energetic charged particles fill the slot region between the inner and outer radiation belts. These suggest that electrons with energies >30 keV penetrate this region, even under levels of modest geomagnetic activity. Those events with sufficient fluxes of particles produce enough ionization to be detected by a ground-based radar in Antarctica; this precipitation lasts for ~10 days on average. Analysis of these data reveals that the average precipitation penetrates to the stratopause (~55-km altitude). For some (if not all) of these events, the likely cause of the most energetic precipitation is an interaction between (relativistic) electrons and plasmaspheric hiss leading to little, if no, local time variation in precipitation. This does not preclude a longitudinal effect given that all radar measurements are fixed in longitude. During winter months the radar is under the stable southern polar atmospheric vortex. This transports atmospheric species to lower altitudes including the ozone destroying chemicals that are produced by energetic precipitation. Thus, the precipitation from the slot region in the Southern Hemisphere will likely contribute to the destruction of ozone and changes to atmospheric heat balance and chemistry; more work is required to determine the true impact of these events.

Plain Language Summary Precipitation of energetic electrons to the atmosphere is both a loss mechanism for radiation belt particles and a means by which the geospace environment influences the Earth's atmosphere; thus, it is important to fully understand the extent of this precipitation. A set of polar orbiting satellites have been used to identify periods when energetic charged particles fill the slot region between the inner and outer radiation belts. These suggest that electrons with energies >30 keV penetrate this region, even under levels of modest geomagnetic activity. Those events with sufficient fluxes of particles produce enough ionization to be detected by a ground-based radar in Antarctica; this precipitation lasts for ~10 days on average. Analysis of these data reveals that the average precipitation penetrates to the stratopause (~55-km altitude). For some (if not all) of these events, the likely cause of the most energetic precipitation is an interaction between (relativistic) electrons and plasmaspheric hiss leading to little, if no, local time variation in precipitation. This does not preclude a longitudinal effect given that all radar measurements are fixed in longitude. During winter months the radar is under the stable southern polar atmospheric vortex. This transports atmospheric species to lower altitudes including the ozone destroying chemicals that are produced by energetic precipitation. Thus, the precipitation from the slot region in the Southern Hemisphere will likely contribute to the destruction of ozone and changes to atmospheric heat balance and chemistry; more work is required to determine the true impact of these events.

1. Introduction

The Earth's radiation belts (or Van Allen belts) are formed by the drift orbits of energetic electrons confined by the Earth's magnetosphere and generally appear as two torus-shaped regions (Van Allen, 1959). The outer belt is highly dynamic, responding strongly to solar wind driving during geomagnetic storms (e.g., Li et al., 1997; Ni et al., 2016; Reeves et al., 1998), occasionally splitting to form two rings (e.g., Baker et al., 2013; Mann et al., 2016, 2018, Shprits et al., 2018). This dynamic nature is controlled by a series of acceleration and loss mechanisms involving interactions with a range of magnetospheric waves (e.g., Horne et al., 2006; Li et al., 2015; Ni et al., 2015; Thorne, 2010; Thorne et al., 2005). The outer belt is separated from the inner by a region known as the slot region; this lies between about L = 2 and

Table 1
POES Satellites Used in This Study With Their Operational Start and End Times (Column 2) and Average Orbital Altitude (Column 3)

Satellite	Operational dates	Altitude (km)
NOAA-15	15 Dec 1998	807
NOAA-16	20 Mar 2001 to 9 Jun 2014	849
NOAA-17	15 Oct 2002 to 10 Apr 2013	810
NOAA-18	30 Aug 2005	847
NOAA-19	2 Jun 2009	870
MetOp-A	21 May 2007	817
MetOp-B	24 Apr 2013	817

Note. POES = Polar Operational Environment Satellites; NOAA = National Oceanographic and Atmosphere Administration.

L = 3. The slot region is generally devoid of energetic electrons and is thought to be formed by a balance between inward radial diffusion and the pitch angle scattering loss of electrons to the atmosphere (e.g., Lyons & Thorne, 1973). This scattering is due to resonant wave-particle interactions with plasmaspheric hiss (e.g., Meredith et al., 2009; Ni et al., 2013).

Although the slot region is typically persistent, during some geomagnetic storms it can be filled by energetic electrons and protons as the outer belt is severely distorted (Baker et al., 2004). One of the biggest examples of such an event occurred during the so-called Halloween storm in 2003; studies suggested that the slot region was filled via a combination of local wave-particle acceleration and inward radial transport (Loto'aniu et al., 2006; Shprits et al., 2006). Electron fluxes remained elevated for several weeks before decaying away and the slot region reforming. Meredith et al. (2009) showed that for the outer slot region ($2.4 < L < 3$) the loss of the relativistic electron flux (2–6 MeV) can be explained via pitch angle scattering by plasmaspheric hiss. Thus, electrons are being scattered into the loss cone and precipitating into the atmosphere.

Precipitating energetic electrons and protons will ionize the neutral atmosphere, increasing the local electron density and driving chemical reactions such as the production of NO_x (N + NO+N3) and HO_x (H + OH + H3; Rusch et al., 1981; Solomon et al., 1981). Both of these gases are catalysts in the reactions that lead to the destruction of ozone, which in turn affects the radiative balance and dynamics of the atmosphere. NO_x is destroyed via photodissociation, and as such, it is long-lived in the darkness of the polar winter and will be transported by the dynamics of the atmosphere. In the winter hemisphere the circulation of winds generates the polar vortex over the polar region, isolating the polar air in the middle atmosphere and drawing it downward; thus, NO_x can be transported to the ozone-rich stratosphere. Seppälä et al. (2007) showed that the Halloween storm led to the production and subsequent descent of significant NO_x levels in the Northern Hemisphere winter. NO_x concentrations in the stratosphere have been shown to be well correlated with geomagnetic activity levels (e.g., Seppälä et al., 2007; Siskind et al., 2000), which in turn has signatures in the dynamics of the stratosphere and polar surface air temperature (Seppälä et al., 2009, 2013).

Thus, energetic charged particle precipitation is potentially important for the dynamics of the middle and lower atmosphere. The energy of the particle is important for determining the altitude profile of NO_x production; the higher the energy, the deeper into the atmosphere a particle can penetrate before being "stopped" (e.g., Rees, 1963). Auroral energy electrons (1–10 keV) will deposit in the lower thermosphere, whereas relativistic energies (~MeV) will penetrate to the lower mesosphere (e.g., Turunen et al., 2009). Due to their larger mass, protons of a given energy will deposit at higher altitudes than the same energy electrons. The atmosphere magnetically connected to the auroral zone and outer radiation belt is a strong source of NO_x during geomagnetic storms, depositing primarily at higher geomagnetic latitudes, though equatorward of the polar cap.

The British Antarctic Survey (BAS) operates Rothera Research Station on Adelaide Island (at 67.57°S 68.13°W) along the Antarctic Peninsula. During the winter months Rothera lies close to or within the polar vortex; due to the offset of the southern geographic and geomagnetic poles, it also lies under the footprint of the radiation belt slot region at L = 2.7. This places it in an ideal location for examining charged particle precipitation from the slot region.

In this paper data from particle detectors on several polar orbiting satellites are used to identify periods of precipitation. These detectors are nominally measuring >30 keV electrons; however, they are also sensitive to MeV energy protons that may be present. The data indicate that moderate to high geomagnetic activity can result in enhanced fluxes of particles in the slot region. Data from a ground-based radar indicate that for events above a given flux threshold there is a significant ionospheric effect. This effect extends to the very lowest altitude of the mesosphere for some events, indicating that high-energy particles, possibly relativistic electrons, are present as well as the moderate energies indicated by the satellites.

2. Instrumentation

2.1. Polar Operational Environment Satellites–Medium Energy Proton and Electron Detector

The Polar Operational Environment Satellites (POES) are operated by the U.S. National Oceanographic and Atmosphere Administration (NOAA). They fly in Sun-synchronous polar orbits with a period of 102 min at altitudes between 800 and 850 km. Table 1 provides a list of the satellites, their lifetimes, and their orbital altitudes. POES carry the Space Environment Module-2 (SEM-2), which includes the Medium Energy Proton and Electron Detector (Evans & Greer, 2004), which measures a range of energies. For this study data have been primarily taken from a telescope pointing approximately in the direction of the magnetic field (0°) measuring the integral electron flux (J_e) above 30 keV, with a cadence of 2 s. This observes electrons that are in the bounce loss cone for when the satellite is poleward of $L \sim 1.5$ (Rodger et al., 2010, Appendix A), but due to the angular size of the detector, only a fraction of the loss cone is sampled. Thus, the measured electron flux may differ from the actual total precipitating flux by as much as 10–15 times depending on geomagnetic activity levels; Rodger et al. (2013) provides a very thorough analysis of this issue.

In this study the POES data have been used to identify slot region filling events. Two-second observations have been averaged to provide daily means and binned as a function of L-shell at 0.1 L resolution. Since the aim of this work is to compare the satellite measurements with a radar at a specific location, it might be reasonable to restrict the POES observations to the same longitude sector as the radar; however, this made no difference to the identification of the slot region filling events beyond increasing the noise in the data.

The SEM electron data also suffer from contamination by energetic protons (Yando et al., 2011) though a technique to remove this contamination has been developed by NOAA (Lam et al., 2010); however, for very energetic protons such as solar protons this routine will not work, and as such during solar proton events (SPEs), data tend to be ignored/removed. Solar protons have energies in the tens to hundreds MeV range and as such tend to precipitate deep into the atmosphere (e.g., Reid, 1974). Their high energies and large gyroradius also allow them to cut across magnetic field lines, until the field becomes too strong for them to penetrate further and they reach a natural cut-off latitude (e.g., Kavanagh et al., 2004; Rodger et al., 2006). This latitude is affected by geomagnetic activity; an increased ring current will weaken the field and lower the cut-off latitude for a given energy proton. In general, the slot region is well removed from the cut-off region for any but the most extraordinarily high energy (and very low flux) protons. However, there is evidence that at the onset of large storms protons can inject much further into the magnetosphere than simple theory predicts (e.g., Lorentzen et al., 2002; Selesnick et al., 2010); this effect and the impact on the data will be discussed in more detail in a later section. The proton data can also be contaminated by the presence of highly energetic electrons (Yando et al., 2011), so caution must be employed when interpreting the satellite data during very energetic events. The P6 proton channel (>6.9 MeV) on POES is susceptible to contamination from electrons with energy in excess of 700 keV (Rodger et al., 2010); however, the P5 channel (0.8 to 6.9 MeV) is not sensitive to contamination, and so a comparison of the two can determine whether P6 is responding to protons or electrons.

In this study the particle data are used only to provide an indication of when a slot region filling event occurs. In principle, it does not matter whether it is electrons or protons that are filling the slot region and then precipitating into the ionosphere, though we will consider whether any identification can be made and the implications for the particle energy depending on which species is responsible.

2.2. Medium-Frequency Radar

The medium-frequency (MF) radar at Rothera (67°S, 68°W) is a coherent, spaced-antenna wind profiler that measures the horizontal neutral winds in the mesosphere and lower thermosphere using the full-correlation analysis technique (Briggs, 1984). The radar transmits a 25-kW pulse at 1.98 MHz, and the reflected signal is sampled on three antennas from 2-km height intervals centered between 56.5- and 102.5-km altitude with a wind profile measurement provided every 102.4 s. The system first operated between 1997 and 1998 and then continuously from 2002. It was initially a joint project between BAS and the University of Colorado and is now a collaboration between BAS and GATS Inc.

As well as providing profiles of the neutral wind in the mesosphere, an MF radar can also act as a qualitative indicator of energetic charged particle precipitation. The radar signal undergoes partial reflection from irregularities in the weakly ionized D-region of the ionosphere that overlaps the mesosphere. This technique

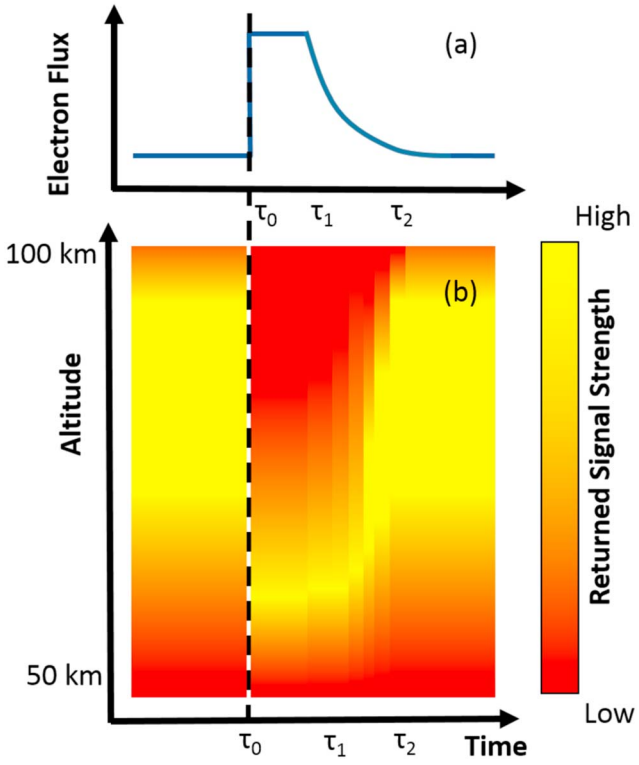

Figure 1. Schematic of the expected response of the signal strength measured by a medium-frequency radar (b) located under a region of precipitation indicated by the blue line in (a). At time τ_0 the precipitation begins instigating a loss of signal at high altitudes; at τ_1 the precipitation begins to reduce until at τ_2 the precipitation is back at pre-event level as is the returned signal strength.

was originally used to probe electron densities in the D-region (e.g., Gardner & Pawsey, 1953) and later applied to wind measurements. Ionization in the D-region causes the attenuation of radio waves in the high-frequency and MF bands, and the level of absorption is different for the ordinary (O) and extraordinary (X) waves. Thus, by measuring interleaved O and X mode returned signals and considering the difference, it is possible to extract the electron density without knowing the full level of attenuation; this is known as the differential absorption technique (e.g., Thrane et al., 1968). An electron density profile can then be used to determine the flux-energy spectrum of precipitating particles (e.g., Semeter & Kamalabadi, 2005), assuming that these are the cause of excess ionization above the background produced by solar radiation.

The Rothera MF radar transmits only the ordinary mode and consequently cannot use the differential absorption technique to determine the electron density and charged particle precipitation. However, by considering changes in the signal-to-noise ratio (SNR) observed by the receive antennas, it is possible to extract an indication of when precipitation is occurring and an estimate of the peak effective energy of precipitation by consideration of the lowest altitude where a change in SNR is measured. An outline of this technique is provided below:

The relationship between the absorption of a signal and the electron density can be derived from the Appleton-Hartree equation for the refractive index (e.g., Davies, 1990) of a collisional plasma and is presented here:

$$A = 4.6\times10^{-5}\int \frac{N_e \nu .dl}{\nu^2 + (\omega \pm \omega_H \cos\theta)^2} \quad (1)$$

where A is the absorption in decibels (dB), integrated along the path through the ionosphere defined by dl, N_e is the electron density (m^{-3}), ν is the effective collision frequency dominated by the electron-neutral collision frequency, ω is the angular frequency of the wave, ω_H is the local electron gyrofrequency, and θ is the angle between the direction of wave propagation and the local magnetic field. If we assume that the collision frequency varies much more slowly than the electron density, N_e and that the propagation is such that $\theta \sim 0$, then we can see that the following is true:

$$A \propto \int N_e .dl \quad (2)$$

If the collision frequency is effectively constant in time, then the absorption is proportional to the electron density at a given height. The assumption of $\theta = 0$ is less valid at the latitude of Rothera than at high latitudes but is reasonable for illustrative purposes. By considering the path of a vertically transmitted signal through the ionosphere and the temporal response of the SNR of the received signal, it is possible to develop a qualitative picture of the effect of varying precipitation on the radar signal.

Figure 1 is a schematic of the predicted response of the radar received power to an increase in precipitating electron flux. Figure 1a gives the time history of the integrated electron flux: The flux increases at time τ_0, remains elevated until τ_1 and then decays back to its original value by time τ_2. This generates an enhancement in electron density in the D-layer that will increase with altitude, the exact profile depending on the flux-energy spectrum of the precipitation. Figure 1b shows the returned signal power of the radar with red (yellow) indicating low (high) returned signal power. Prior to τ_0, there is low power in the lowest altitudes and high power above; the electron density is higher with increased stronger irregularities/gradients to scatter from at the higher ranges. After τ_0, there is a change as the power increases in the lower altitude gates in response to the increased electron density; the path described in equation (2) is relatively short, and so there is small absorption. At higher altitudes the signal fades away as the transmitted and reflected waves have to pass through a larger portion of more enhanced electron density such that the integrated path is large and

the absorption given by equation (2) will also be large. Between τ_1 and τ_2 there is a shift back to preonset conditions, as the power reduces in the lower range gates and increases higher up.

The following section details how events were selected from the data.

3. Observations

3.1. Event Selection

Fifty-four separate slot region filling events were identified between 2002 and 2014 in the >30 keV electron flux, J_e. The criteria applied to determine the events were as follows: (i) an increase in flux at L = 2.7 of at least 40 $cm^{-2}{\cdot}s^{-1}{\cdot}sr^{-1}$ and (ii) an identifiable enhancement that included the range of the outer belt and extended in L-shell to the edge of the inner belt. To determine the 40 $cm^{-2}{\cdot}s^{-1}{\cdot}sr^{-1}$ limit, we calculated the distribution of the difference between successive points (the approximate first derivative) to identify the noise level of the daily average. The distribution was Gaussian around 0 to ±30 $cm^{-2}{\cdot}s^{-1}{\cdot}sr^{-1}$, characteristic of noise, such that 40 $cm^{-2}{\cdot}s^{-1}{\cdot}sr^{-1}$ should be above the noise level. This limit essentially acts as a filter to reduce the data that were subsequently assessed for an increase across the wider range of L-shells; the limit was kept deliberately low to minimize any selection bias, whereby we might dismiss weaker events. In principle, 40 $cm^{-2}{\cdot}s^{-1}{\cdot}sr^{-1}$ results in an initial pool of 472 potential events; raising the limit to 60 produces a pool of 319 potential events. However, in practice, raising the limit to 60 reduced the number of viable events by 7, and raising it to 80 $cm^{-2}{\cdot}s^{-1}{\cdot}sr^{-1}$ removes an additional four events—a reduction in the data set of ~20%. Each event was inspected for data quality in the two instruments, and five events were discarded, leaving 49 events in total. These 49 events are listed in Table 2 and are indicated by the black vertical arrows in Figure 2e.

Figure 2 shows the daily averaged data from the POES satellites for selected electron and proton channels (a–e) and the 1-min SYM-H index for geomagnetic context. The top two panels show the >30-keV electron flux (J_e) from (a) the 90° telescope and from (b) the 0° telescope. The next two panels show the >6.9-MeV proton flux (J_p) from the (c) 90° telescope and the (d) 0° telescope. The y-axis gives the L-shell of the observation; this is the McIlwain L-shell, which assumes a simple dipole field, a reasonable assumption in the inner magnetosphere. The altitude of the POES orbit is such that the satellites are sampling particles that are mirroring far away from the equator and as such do not capture the full trapped population in the 90° telescopes. As discussed above, the 0° telescopes are measuring the precipitating flux, but it is unclear whether they capture the full distribution. The plots are limited at L = 6 though POES measure to larger L-shells. Similarly, the electron fluxes have been allowed to saturate in the plot in order to show the weaker electron fluxes that occur in the slot region. The electron measurements show the day-to-day variability of flux in the outer belt with occasional strong enhancements across the whole range of L; this is clear in the precipitating flux as well though the background is much lower. The proton flux, particularly the precipitating flux, is much lower than the electron flux, but it also show enhancements across all L-shells; however, not all such events show up as the proton flux descends into the detector noise level.

Figure 2e shows J_e for both the trapped (red line) and precipitating (blue line) detectors at L = 2.7. Figure 2f displays the 5-min SYM-H index taken from the OMNI data set from 2002 to 2014 inclusive (https://omniweb.gsfc.nasa.gov/ow_min.html). SYM-H is derived from midlatitude magnetic data and represents the longitudinally symmetric disturbance in the direction of the dipole-pole; this is similar to the Dst index (Sugiura & Poros, 1971) but is derived from different stations in a slightly different coordinate system. Essentially, it is an index that represents the level of geomagnetic storm activity.

The diamonds in each of the panels indicate the times of event identification; a significant fraction of these occur around the time of decreases in the SYM-H. Some detail of these events can be gleaned from Figure 2b: There is an increase in flux that stretches from the outer belt at high L to the inner belt, filling the slot region. The magnitudes of these events vary in flux and occur across a range of SYM-H values. The majority of events occur in the first few years when geomagnetic activity was highest in the descending phase of the solar cycle (see the density of diamonds in up to 2006 compared with 2006 to 2011). There is a correspondingly strong signal in the proton flux for a number of these events, but not all. This will be discussed in a later section. The full list of these events can be seen in Table 2 along with a number of additional parameters that will be discussed in later sections.

Table 2
List of Identified Slot Region Filling Events, Including the Peak Electron and Proton Flux Characteristics from POES, and Details of Concurrent Solar Proton Events

	Peak POES electron flux ($cm^{-2}{\cdot}s^{-1}{\cdot}sr^{-1}$)		SPE			POES proton flux ($cm^{-2}{\cdot}s^{-1}{\cdot}sr^{-1}$)			
Epoch	0° J_e	0° ΔJ_e	Start	Peak	Peak >10 MeV flux ($cm^{-2}{\cdot}s^{-1}{\cdot}sr^{-1}$)	90° J_p at peak SPE	peak 90° J_p	90° J_p at min. SYM-H	Min. SYM-H (nT)
2002-04-18	601	464	2002-04-17	2002-04-17	24	17	375	33	−151
2002-05-22	497	230	2002-05-22	2002-05-23	820	29	38	33	−113
2002-09-06	728	541	2002-09-07	2002-09-07	208	33	50	33	−167
2002-10-01	977	738	—	—	0	0	604	346	−153
2003-02-03	627	434	—	—	0	0	67	67	−79
2003-03-30	356	133	—	—	0	0	54	21	−89
2003-04-30	386	148	—	—	0	0	71	50	−93
2003-05-12	460	209	—	—	0	0	96	67	−26
2003-05-28	1,289	1,085	2003-05-28	2003-05-29	121	42	727	238	−152
2003-06-17	791	457	2003-06-18	2003-06-19	24	196	196	96	−162
2003-07-11	565	294	—	—	0	0	79	58	−125
2003-08-17	941	613	—	—	0	0	1,123	108	−138
2003-10-14	364	214	—	—	0	0	29	29	−102
2003-10-23	539	320	2003-10-26	2003-10-27	466	42	79	67	−70
2003-10-28	51,488	51,251	2003-10-28	2003-10-29	29,500	742	6,167	6,167	−363
2003-11-19	126,631	126,122	2003-11-21	2003-11-22	13	2,254	2,254	171	−488
2003-12-04	437	233	2003-12-02	2003-12-02	86	146	129	129	−60
2004-01-22	434	184	—	—	0	0	96	29	−137
2004-02-10	409	245	—	—	0	0	33	33	−107
2004-03-10	351	211	—	—	0	0	42	4	−101
2004-04-05	272	119	2004-04-11	2004-04-11	35	29	54	21	−96
2004-07-24	2,537	2,387	2004-07-25	2004-07-26	2,086	904	2,288	88	−166
2004-11-07	39,120	38,976	2004-11-07	2004-11-08	495	3,188	12,200	3,188	−393
2005-01-17	851	530	2005-01-16	2005-01-17	5,040	71	221	121	−107
2005-05-07	600	450	—	—	0	0	192	29	−115
2005-05-14	3,501	3,111	2005-05-14	2005-05-15	3,140	158	735	158	−302
2005-05-28	569	222	—	—	3,140	0	113	54	−43
2005-07-13	496	287	2005-07-14	2005-07-15	134	38	46	33	−56
2005-08-23	2,136	1,934	2005-08-22	2005-08-23	330	25	692	129	−174
2005-09-10	775	437	2005-09-08	2005-09-11	1,880	133	588	133	−135
2006-04-13	493	312	—	—	0	0	83	33	−110
2006-12-14	602	422	2006-12-13	2006-12-13	698	29	146	58	−206
2007-07-24	433	248	—	—	0	0	63	46	−9
2008-03-31	408	224	—	—	0	0	46	54	−21
2009-07-21	194	43	—	—	0	0	54	54	−93
2010-04-04	244	108	—	—	0	0	58	50	−66
2010-05-30	247	94	—	—	0	0	54	50	−57
2010-08-08	269	110	—	—	0	0	58	38	−31
2011-05-24	236	93	—	—	0	0	54	33	−12
2011-07-07	287	124	2011-07-07	2011-07-07	72	33	46	38	−27
2011-08-04	371	227	2011-08-04	2011-08-05	96	63	63	46	−104
2011-09-09	227	90	—	—	0	0	71	33	−76
2011-09-25	284	104	2011-09-26	2011-09-24	35	46	46	46	−111
2011-10-25	348	205	—	—	0	0	42	42	−160
2012-04-24	337	159	—	—	0	0	71	71	−125
2012-07-07	396	242	2012-07-07	2012-07-07	25	46	46	25	−9
2012-10-01	269	113	2012-09-28	2012-09-28	28	33	54	38	−138
2013-01-30	307	154	—	—	—	—	—	—	−11
2013-04-16	372	218	2013-04-11	2013-04-11	114	33	58	29	−18

Note. Column 1 gives the epoch dates and times for each of the 49 identified slot region filling events. Columns 2 and 3 are the >30-keV electron flux from the 0° telescope on POES and the relative change in flux from the pre-event to the peak for each event, respectively. Columns 4–6 show the start and peak times and the peak flux (at >10 MeV) for any SPE that occurred during or before the slot region filling event, respectively. Columns 7–9 show the >6.9-MeV proton flux from the 90° telescope on POES for the time of peak SPE, peak electron flux, and day of minimum SYM-H during the events. The final column gives the value of the minimum SYM-H recorded during the events. POES = Polar Operational Environmental Satellites; SPE = solar proton event. Dates are formatted as year-month-day.

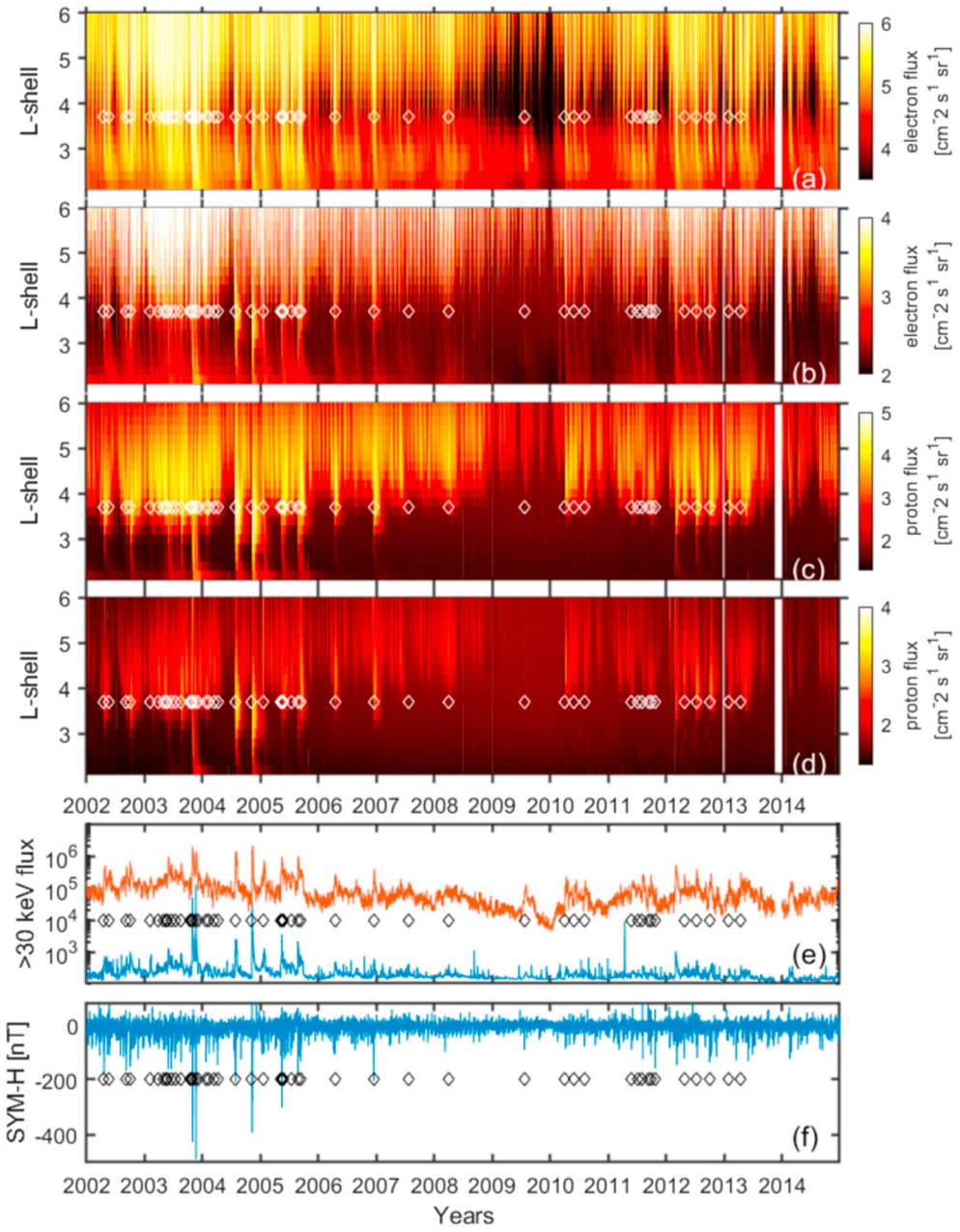

Figure 2. Daily averages of selected integral charged particle flux ($cm^{-2}{\cdot}s^{-1}{\cdot}sr^{-1}$) measured by the SEM instrument on the POES satellites, limited between L = 2.2 and L = 4, from 2002 to 2014 inclusive. Data are from (a) the >30-keV electron 90° telescope, measuring the trapped population; b) the >30-keV electron 0° telescope, sampling the bounce loss cone; (c) the 90° trapped proton flux for energy >6.9 MeV; and (d) the 0° precipitating proton flux at >6.9 MeV. (e) The >30-keV electron flux at L = 2.7 for the trapped (red) and precipitating (blue) detectors. (f) The SYM-H index for the same time period. Each of the diamonds in each of the panels shows the times of a slot region filling event; these match up with the large flux enhancements in (a) to (e). POES = Polar Operational Environment Satellites; SEM = Space Environment Module.

Figure 3 shows daily median SNR values from receiver 3 of the MF radar from March 2002 to December 2014. There are two patterns: (i) a seasonal variation in the SNR and (ii) a long-term change in the SNR. The seasonal variation is due to changes in solar illumination; the signal scatters from gradients in the ionized atmosphere, and as there is increased ionization at lower altitudes in the summer months, we observe a greater response from those height ranges than in winter. The cause of the long-term change is more difficult to determine; it might be a solar cycle effect, but we cannot say with certainty without a longer data set given the recent long

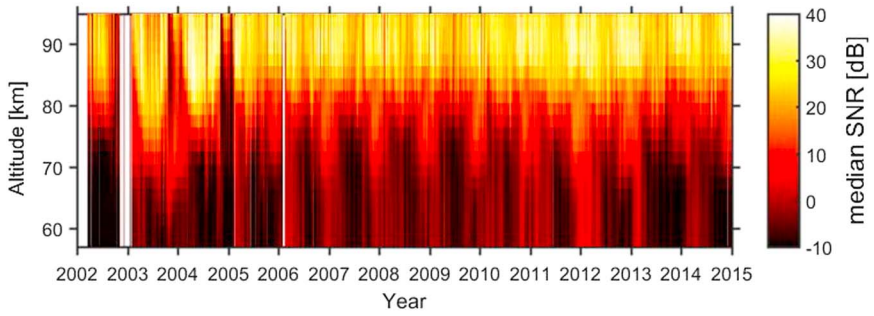

Figure 3. Signal-to-noise ratio (SNR) from receiver 3 of the medium-frequency radar at Rothera from March 2002 to December 2014 inclusive, measured in decibels. Daily median values in each range gate are presented, showing a long-term variation and the seasonal cycle.

solar minimum. For this study it is enough to identify that there is a climatology in the SNR that must be taken into account when looking at events dispersed in time through the data set.

3.2. Event Examples

Figure 4 shows an example of a slot region filling event that occurred on 2 October 2002. Figure 4a shows the daily mean of J_e at L = 2.7. The flux rises to 980 $cm^{-2}{\cdot}s^{-1}{\cdot}sr^{-1}$ on 2 October 2002, from a background of 300 $cm^{-2}{\cdot}s^{-1}{\cdot}sr^{-1}$ in the preceding days. The flux slowly decayed to pre-event levels over the next 20 days, with three minor increases occurring on 6, 13, and 18 October 2002; each of these consisted of an increase of between 150 and 200 $cm^{-2}{\cdot}s^{-1}{\cdot}sr^{-1}$ but did not fulfill the event selection criteria on their own.

Figure 4b shows the hourly medians of the SNR from the MF radar between 55- and 95-km altitude (2-km range gates); as the electron flux rises, it is accompanied by a reduction in SNR at the higher altitudes (above ~70 km) and an increase in SNR below 65 km, following the pattern outlined in Figure 1. However, there is a diurnal variation in the SNR such that the change is restricted to certain times of day. Figure 4c shows the solar elevation angle for the location of the MF radar; at the day of event onset the Sun lies at 25° above the horizon at local noon and 20° below at midnight. The maximum effect on the SNR occurs at noon, with the minimum at midnight. The lack of sunlight in the mesosphere has two main effects:

1. The reduction in solar ionization reduces the overall electron density. This can be seen in a standard diurnal variation in the MF radar SNR data (e.g., Figure 4 prior to event onset). At those latitudes where it can occur, charged particle precipitation becomes the dominant mechanism of ionization.
2. In darkness, attachment of electrons to neutral species increases such that the mesospheric plasma is made up of ions, electrons, and negative ions (e.g., Kavanagh et al., 2004; Rietveld & Collis, 1993). Negative ions do not contribute to radio absorption, so the MF radar signal experiences less attenuation. The associated reduction in electron density (and growth in negative ion density) results in a reduction of radar targets, which in turn particularly reduces the SNR in the lower range gates.

The strong reduction in SNR above 75 km persists for the duration of the elevated flux, though there is a change in the altitudinal profile as time progresses. After 11 October 2002, the effect is much less pronounced, in terms of both the lower altitude enhancement and the reduction at higher range gates. By the end of the event the solar elevation angle at midnight has raised to −10° with the Sun spending a shorter time below the horizon.

3.3. Superposed Epoch Analyses

In this section a superposed epoch analysis of the MF radar SNR is presented. To compare the SNR with the daily averages of electron fluxes from POES, an hourly median value centered on local noon is used; this minimizes the impact of solar ionization (or lack thereof) on the SNR. The results do not qualitatively change if a full daily median (or mean) is used.

For the analysis the epoch is defined as the day immediately preceding the increase in flux, and 20 days before and 20 days afterward are presented. The MF radar data have been normalized to account for the underlying climatology to enable a direct comparison between events and minimize the dominance of

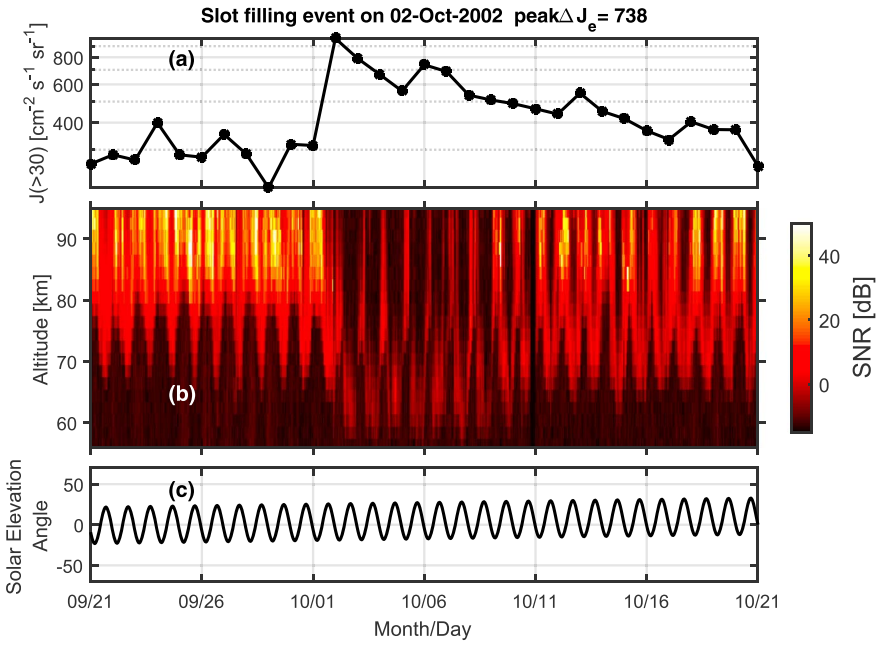

Figure 4. Example of a slot region filling event that began on 2 October 2002. (a) The integral electron flux for energies >30 keV from the 0° detector (J_e), with a clear enhancement on 2 October 2002 that persisted for several days. (b) The corresponding signal-to-noise ratio (SNR) from the medium-frequency radar at Rothera. There is a diurnal variation that changes once the precipitation begins, switching from high (low) SNR during the day (night) to a much weaker daytime signal compared to nighttime. (c) The solar elevation angle at the site of the radar for this period.

extreme cases. This was achieved by determining the 2 days with the lowest J_e within the 5 days prior to each event and calculating the corresponding median SNR at all altitudes. The resultant profile represents the quiet period prior to any precipitation occurring and is subtracted from all days within the analysis period for the given event. Thus, rather than analyzing the SNR, it is actually the difference in SNR that is being considered, denoted as ΔSNR. The same process was followed for J_e to produce ΔJ_e, that is, J_e minus the minimum flux prior to the epoch. This provides a baseline for all events to be compared against each other.

The 5-day span for determining the quiet period was chosen after considering the temporal distribution of the slot region filling events: One pair of events was separated by 5 days with a further four pairs within 15 days of each other, and nine pairs occurred within 20 days. Given that the flux can remain elevated for over 20 days using a short period like 5 days prior to the onset to determine the undisturbed quiet values is sensible.

Figure 5 shows the results of the superposed epoch analysis of all 49 events. Figure 5a shows the median ΔSNR, as a function of altitude, for all events from 20 days prior to the epoch to 20 days afterward. Figure 5b displays the median J_e (solid black line) for the same time range, with the upper and lower quartiles of the underlying distribution (dashed lines). This is the flux measured by the 0° telescope indicating precipitation. Following the epoch, there is a step in J_e with the median rising from a minimum of J_e = 190 $cm^{-2}{\cdot}s^{-1}{\cdot}sr^{-1}$ to a peak of 400 $cm^{-2}{\cdot}s^{-1}{\cdot}sr^{-1}$ (ΔJ_e = 210 $cm^{-2}{\cdot}s^{-1}{\cdot}sr^{-1}$). The interquartile range peaks at 350 $cm^{-2}{\cdot}s^{-1}{\cdot}sr^{-1}$ on day 5, which illustrates the wide distribution of flux increases within the 49 events (can also be seen in Table 2). The median flux remains elevated above the pre-epoch levels until the end of the period presented, but by day 15 it has dropped to 260 $cm^{-2}{\cdot}s^{-1}{\cdot}sr^{-1}$, which is a change of 66% of the difference between the peak and the pre-event level.

Figure 5a shows that there is a sharp change in ΔSNR following the epoch. Above 72.5 km there is a reduction in ΔSNR that lasts for 11 days before approaching pre-event levels. Below 66.5 km the ΔSNR increases for the initial 5 days. The greatest change occurs within the first 6 days, possibly associated with the more extreme events as there is a corresponding bump in the upper quartile of the flux shown in Figure 5b. The average increase in ΔSNR below 66.5 km during the first 5 days was 2.1 ± 0.7 dB, whereas above 72.5 km ΔSNR reduced by −6.5 ± 2.3 dB in the same period.

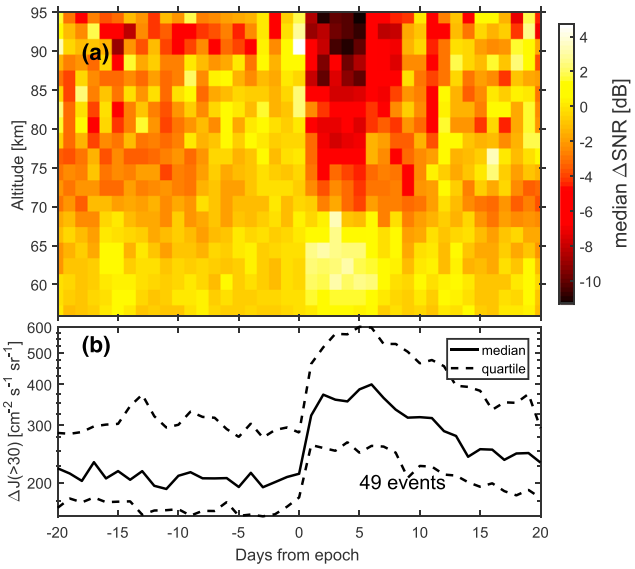

Figure 5. A superposed epoch analysis of all 49 slot region filling events. The zero epoch is defined as the day prior to an increase in >30-keV electron flux. Data are shown for 20 days before and after the epoch. (a) The change in signal-to-noise ratio (ΔSNR) relative to a quiet period prior to event onset; the daily values represent the median SNR from around noon in magnetic local time. (b) The corresponding change in >30-keV electron flux (ΔJ_e); the black line is the median response, and the two dashed lines show the interquartile range of the data.

Table 2 shows that there is a spread of peak fluxes throughout the 49 slot region filling events. These included notably large geomagnetic storms, such as the Halloween storm in 2003, as well as the previously noted events that take place during much quieter geomagnetic conditions. The superposed epoch analysis presented in Figure 5 is a mixture of all of these events with no regard for the intensity of individual slot region injections. To establish whether there is a lower limit on the ionospheric effect of the events, a series of epoch analyses were performed using subsets of the events limited by values of ΔJ_e. Care must be taken as introducing limits significantly reduces the number of events in each analysis.

Figure 6 shows the ionospheric response to different ranges of ΔJ. Figures 6a1–6a4 show the results of the superposed epoch analyses of the ΔSNR for the cases where (a1) $\Delta J_e < 150$ cm^{-2}·s^{-1}·sr^{-1}, (a2) 150–300 cm^{-2}·s^{-1}·sr^{-1}, (a3) 300–800 cm^{-2}·s^{-1}·sr^{-1}, and (a4) $\Delta J_e > 800$ cm^{-2}·s^{-1}·sr^{-1}. Figures 6b1–6b4 show the associated superposed epoch analyses of the electron flux. These limits were chosen to retain a reasonable number of events in each group while providing a means of investigating any transition from noneffective or weakly effective to strongly effective fluxes. The ΔJ_e data in Figures 6b1–6b3 have been plotted on the same scale to illustrate the differences in the levels of precipitation. Due to the large values of ΔJ_e in the fourth group (Figure 6b4) this panel uses an expanded Y-scale.

The median ΔSNR shown in Figure 6a1 is composed of 12 events and is variable throughout. There is a hint of a response above 74.5 km, but it fits with the variability of the rest of the period. Similarly, in Figure 6a2 there is no strongly visible response to the precipitation below 84 km and the change above is not dissimilar to the level of variability at other times. This ΔSNR is composed of 18 events.

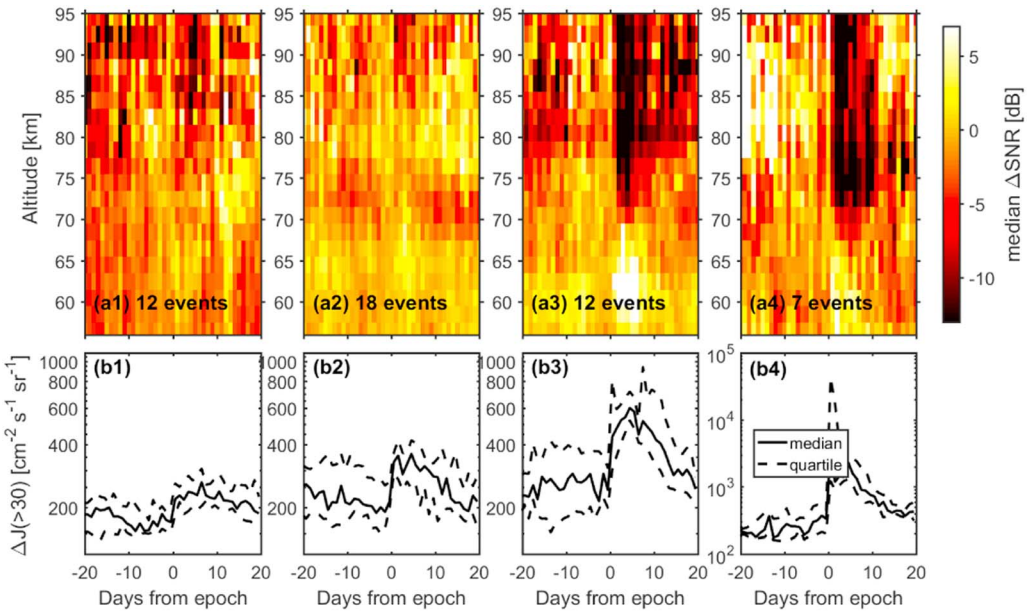

Figure 6. Superposed epoch analyses for four subsets of the data. The data binning was selected to balance different electron flux levels while maintaining a reasonable number of events in each subset. The top row of panels show the median change in signal-to-noise ratio (ΔSNR) for (a1) $\Delta J_e < 150$ cm^{-2}·s^{-1}·sr^{-1}, (a2) $150 < \Delta J_e < 300$ cm^{-2}·s^{-1}·sr^{-1}, (a3) $300 < \Delta J_e < 800$ cm^{-2}·s^{-1}·sr^{-1}, and (a4) $\Delta J_e > 800$ cm^{-2}·s^{-1}·sr^{-1}. The bottom row of panels (b1 to b4) show the corresponding values of ΔJ_e (black lines) and the associated interquartile ranges.

Figure 6a3 shows the result of limiting the events to those with a flux difference between 300 and 800 $cm^{-2}{\cdot}s^{-1}{\cdot}sr^{-1}$ (10 events). In this instance, there is a response in ΔSNR on day 1; there is a –12-dB reduction above 72.5 km by day 2. At lower altitudes there is an increase (between 58 and 70 km) of at least 5 dB in the ΔSNR. This lower altitude change recovers quickly (7 days) compared to the higher attitude change, which takes about 12 days to reach pre-event levels.

In the final two panels (Figures 6a4 and 6b4) the events are limited to those with $\Delta J_e > 800$ units (seven events). The interquartile range in Figure 6b4 shows that there is a large spread of flux. Figure 6a4 shows that once again we have a response following the epoch; there is a reduction in ΔSNR above 70 km, possibly extending lower. There are hints of an enhancement in ΔSNR, but it is not as well defined as in the previous case (Figure 6a3). The temporal structure seems somewhat different for these events with a slightly shorter response; this reflects the flux in Figure 6b4 that drops away from the peak value slightly quicker.

3.4. Significance Testing

To test the significance of the changes in ΔSNR presented in Figures 5 and 6, a series of two-sided Kolmogorov-Smirnov (KS) tests were performed (Kolmogorov, 1933; Smirnov, 1948). For every altitude and every time relative to the epoch, the underlying distribution of ΔSNR is compared against a randomly sampled distribution drawn from the SNR data set; the null hypothesis is that the two distributions are drawn from the same underlying continuous population. This was repeated with 100 random sets of 100 epochs for each of the cases presented in Figures 5 and 6, and we recorded the percentage of those where the KS test indicated that the null hypothesis could be rejected at the 5% confidence level.

Figure 7 presents the results of the KS tests for the cases of: (a) $\Delta J_e > 0$, (b) $\Delta J_e < 150$, (c) $150 < \Delta J_e < 300$, (d) $300 < \Delta J_e < 800$, and (e) $\Delta J_e > 800$. Results are shown as a function of altitude (*y*-axis) and day from epoch (*x*-axis); the color scale gives the percentage of tests where the 95% significance level was exceeded (i.e., $p < 0.05$).

Figure 7a, which represents all 49 events, shows that following the epoch, there is a significant difference at nearly all altitudes that lasts for ~5 days. This suggests that the response to the slot region filling on the SNR data is real. The remaining panels break this result down by considering the same subsets as presented in Figure 6, based on flux limits.

Figures 7b and 7c show no evidence of a significant response. This suggests that a change in flux of less than 300 $cm^{-2}{\cdot}s^{-1}{\cdot}sr^{-1}$ is unlikely to prompt a response in the SNR of the radar; this is likely due to too low levels of additional ionization. In Figure 7c there is a small clustering of high percentages following day 3; however, this is similar to the cluster at day 10 and as such cannot be taken as a response to the event onset. It is worth noting that the limits for binning the data were chosen in an attempt to provide a measure of balance to the sample numbers for the epoch analysis while keeping the flux levels as similar as possible in each bin. Therefore, it is possible that individual events with ΔJ_e close to 300 $cm^{-2}{\cdot}s^{-1}{\cdot}sr^{-1}$could have a small effect in the SNR that this analysis is not revealing. In general, though, this is not the case.

There is a large swathe of significant values in Figure 7d, immediately following the epoch and lasting for at least 7 days at 64.5 km and 12 days, perhaps as long as 18, at 80.5 km. This corresponds to the 10 events with $300 < \Delta J_e < 800$, displayed in Figure 6a3. It would appear that most of the structure in Figure 7a, which looks at all events, is caused by this set of events. The final panel (Figure 7e) contains the most intense events ($\Delta J_e > 800$ $cm^{-2}{\cdot}s^{-1}{\cdot}sr^{-1}$); the range of fluxes that contribute to this sample set is very large as can be seen in Figure 6b4. The KS testing resulted in a significant change above 68.5 km, which lasted for 12 days at 80.5 km. Below 68.2 km there is no significant difference; this result is counterintuitive given the strong response shown in Figure 6a4. This may be caused by a mixture of several factors: These intense events may have an energy spectrum heavily skewed toward the lower end of J_e, that is, much higher fluxes at the lower energies; the low number of samples with a large variability of ΔJ_e could have an effect; and for these larger events there could be significant numbers of precipitating protons that will both lead to an overestimate of J_e and produce a very different ionization profile. This latter issue will be discussed in a later section.

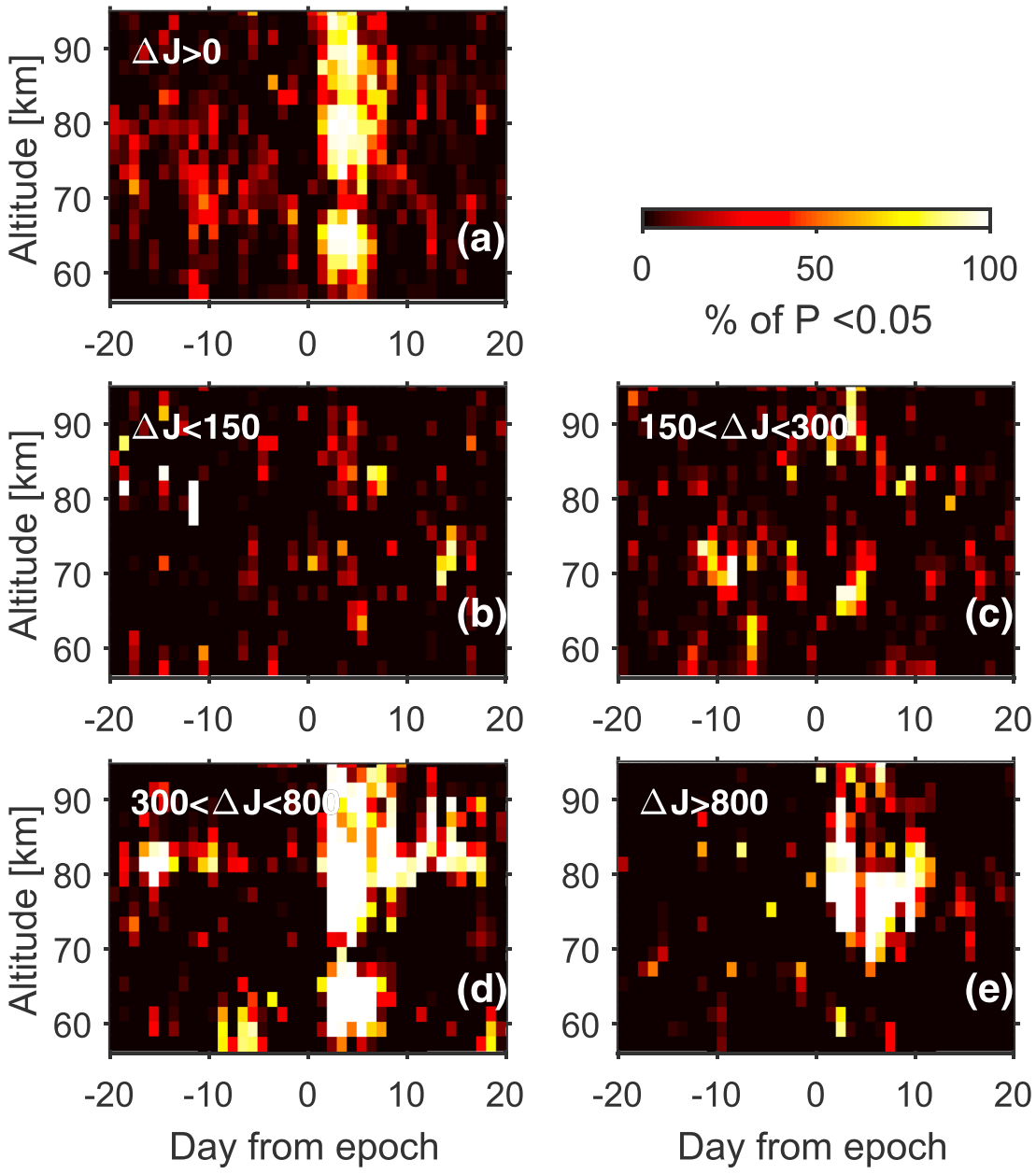

Figure 7. Results of a set of Kolmogorov-Smirnov tests on the medium-frequency radar change in signal-to-noise ratio (ΔSNR) for (a) all 49 events and (b–e) each of the subsets described in Figure 6. The null hypothesis is that the samples are drawn from a different distribution. Each of the sets of ΔSNR data was tested against a random set sampled from the medim-frequency radar data set; this was repeated 100 times for each set of data. The percentage of times that the Kolmogorov-Smirnov test returned a *p* value of less than 0.05 were recorded and are presented.

4. Discussion

4.1. Response to Geomagnetic Activity

Figures 6 and 7 show that the 49 slot region filling events that have been identified fall into two categories: those events that have zero effect on the ΔSNR of the MF radar ($\Delta J_e < 300$ cm^{-2}·s^{-1}·sr^{-1}), comprising the two lower flux sets, and those that have a clear effect ($\Delta J_e > 300$ cm^{-2}·s^{-1}·sr^{-1}), comprising the two higher flux sets (including the extreme events). For ease of reference these two groups will be referred to as "ineffective" and "effective," respectively, in the discussion, though the four flux groupings will also occasionally be referred to when appropriate.

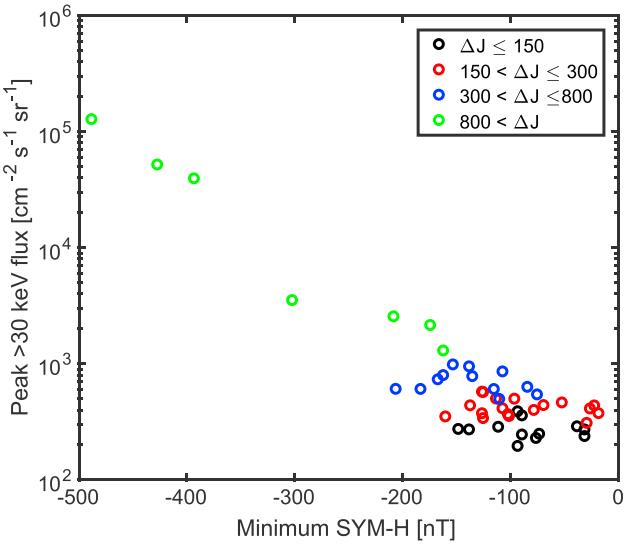

Figure 8. Plot of the peak >30-keV electron daily flux as a function of geomagnetic activity represented by the SYM-H index. Each circle represents a single slot-filling event. They are color coded by the flux difference (the difference between the peak value and the minimum value in the days preceding event onset) and grouped into the same subsets as in Figure 6.

All of the events occurred against a background of varying geomagnetic activity levels as indicated by the SYM-H index (Figure 2). Figure 8 shows the peak flux for each event at $L \sim 2.7$ plotted as a function of the minimum SYM-H value within the 3 days following the epoch. Since observations took place predominantly during the extended solar minimum and a relatively weak solar maximum, there are not many very large storms in the data set; 39% of events occurred for SYM-H > -100 nT, and another 49% lie between -100 and – 200 nT, leaving six events (12%) for SYM-H < -200 nT.

In Figure 8, each event is color coded to indicate the ΔJ_e regime to which they belong. There is a linear correlation between the two variables: High peak fluxes tend to be associated with the most intense storms. However, there is a considerable overlap in SYM-H for those events with $\Delta J_e > 800$ cm^{-2}·s^{-1}·sr^{-1}: -18 to 160 nT for the ineffective events and – 75 to -206 nT for the effective. The high ΔJ_e events (green circles) follow a linear trend and occur for SYM-H ≤ -162. This clustering of events suggest that even though high geomagnetic activity can lead to slot region filling, sustained events can occur even in the absence of strong storm conditions. Park et al. (2010) identified a non-storm-time injection of electrons and protons into the slot region that they associated with substorm activity. This event occurred on 24 February 2004 and lasted for less than a day; consequently, it was not included in the events identified here. Park et al. (2010) suggested that the mechanism behind the injection could be connected to a localized enhancement of the substorm electric field (after Ganushkina et al., 2000) and/or enhancements in ultralow-frequency wave activity (e.g., Liu et al., 2003). Recent work by Califf et al. (2017) has confirmed that an enhancement in the convection electric field can lead to the energization and transport of electrons up to 500 keV in the slot region.

4.2. Electron Versus Proton Precipitation

It is not possible with the MF radar to discriminate whether the changes in ionization that cause the change in SNR are due to proton or electron precipitation. As mentioned in section 2.1, the POES electron data suffer contamination from solar protons and at the same time the presence of high-energy electrons will lead to a false reading in the >6.9-MeV proton detector (designated as P6; e.g., Evans et al., 2008; Yando et al., 2011).

Figures 2c and 2d show the >6.9-MeV proton flux (J_p) from years 2002 to 2014 inclusive. There are clear examples where J_p shows a similar signature to J_e; however, this is only the case for those events with a large SYM-H value and does not occur for all events.

Columns 5 to 7 of Table 2 provide information on SPEs that occur around the slot-filling events. Column 5 gives the start time of the SPE, when the >10-MeV proton flux measured in geostationary orbit by the GOES (Geostationary Operational Environmental Satellites) satellites surpasses 10 cm^{-2}·s^{-1}·sr^{-1}. Column 6 gives the time of maximum >10-MeV flux, and column 7 gives the corresponding flux value. These values were obtained from the list (ftp://ftp.swpc.noaa.gov/pub/indices/SPE.txt) maintained by the NOAA Space Weather Prediction Center.

Solar protons (with energies greater than MeV) will cross magnetic fields lines and penetrate the magnetosphere; the extent is dependent on their energy, and eventually, they will reach a cut-off L-shell, beyond which they cannot travel. These cut-offs are dependent on the magnitude of the magnetic field, and during storms when the ring current is enhanced this can lead to a weakening in the field and suppression of the cut-off, allowing protons to cross to lower L-shells. Kress et al. (2004) used particle simulations to show that protons with energy >25 MeV could access within $L = 4$ when there is a high-density solar wind impulse acting on the magnetosphere. This matched observations of proton injections into the slot region during the 24 November 2001 storm made by the Highly elliptical orbit (HEO) 1997-068 (also known as HEO-3) spacecraft. Thus, for events with a large SYM-H (indicating enhanced ring current) that coincide with an SPE there is a likelihood that energetic protons are also being injected into the slot region.

Of the 49 slot region filling events, 25 did not occur with or during an SPE (just over 50%). For the remaining 24 events the peak >10 -MeV flux measured at geostationary orbit can be compared with the flux of >6.9-MeV protons (J_p) measured by POES on the same day. In general, there is a slight tendency for the higher POES flux to correspond with the higher GOES flux; however, the two parameters are not strongly correlated ($R = 0.1$), with significant scatter. Thus, it is not compelling evidence that the ionization changes detected by the MF radar are consistently caused by the precipitation of newly injected protons.

Selesnick et al. (2010) used detectors on the HEO-3 satellite to study the flux of protons with energies between 27 and 45 MeV, earthward of $L = 4$. The HEO-3 satellite is in a highly elliptical orbit, and measurements were made close to perigee, which at the start of 2002 was at ~1.31 Earth radii, or ~1,900-km altitude, but was moving earthward such that by mid-2002 it was at ~1,800-km altitude. This is approximately double the orbital altitude of the POES (see Table 1). The paper presented observations between 1998 and 2005 (inclusive) providing 4 years of overlap with our data set and covering 17 of the SPEs; of the remaining six, only one had significant peak flux at geostationary orbit and was associated with a SYM-H value that could suggest a suppressed cut-off. Figure 2 of Selesnick et al. (2010) shows the extent of L reached by the 27- to 45-MeV protons and only two of the events between 2002 and 2005 directly penetrated within $L = 3$: 29 October 2003 (event 15 in Table 2) and 7 November 2004 (event 23 in Table 2). The former is the well-known Halloween storm (e.g., Baker et al., 2004), where studies have shown that the slot region contains energetic electrons following the storm onset as well as protons. The latter was not such a large SPE (in terms of the peak flux), but both of these events were toward the top end of the distribution of J_e events.

The event on 7 November 2004 recorded a value of $J_p = 3{,}188$ cm^{-2}·s^{-1}·sr^{-1} on the day the SPE reached its peak, subsequently rising to 12,200 cm^{-2}·s^{-1}·sr^{-1}. This coincided with $J_e = 39{,}120$ cm^{-2}·s^{-1}·sr^{-1}, and it might be assumed that the electron channel is being contaminated. However, the POES proton fluxes are much higher than the peak >10 MeV measured by GOES at geostationary orbit (496 cm^{-2}·s^{-1}·sr^{-1}). This discrepancy seems too large to simply be due to a difference in calibration between the two detectors. It seems likely that the high J_p flux is actually due to contamination by energetic electrons (>700 keV). Unfortunately, a comparison with the lower-energy proton channel, P5, will not be conclusive in this case: If the geomagnetic cut-off is not sufficiently suppressed, the lower-energy protons will not penetrate to these low L-shells.

As well as directly identifying the SPE penetration, Selesnick et al. (2010) identified events where the proton flux increased and decreased significantly; this included two SPEs on 8 September 2005 and 16 January 2005 that coincided with events 30 and 24, both of which recorded high J_p from POES, suggesting that they included significant proton fluxes. One noteworthy increase identified by those authors occurred prior to the onset of our data set; on 23 November 2001 there was a large SPE associated with a large increase of flux in the slot region, effectively swelling the inner proton belt (see Figure 1 of Selesnick et al., 2010) beyond $L = 2.7$. According to the HEO-3 data, the belt remained swollen until the Halloween storm in October 2003, which caused a significant loss of protons. Throughout this period the omnidirectional flux of protons was between approximately 4 and 20 protons/s; the authors opted to use these unnormalized data units throughout due to an uncertainty with the sensor geometry factor (~0.5 cm^2 sr).

Over the same time interval the POES proton data do not record an increase in the background flux. There is also no corresponding signal in the electron flux, and so it is unlikely to be having a significant contamination effect. Zou et al. (2011) used the omnidirectional proton detectors on the POES spacecraft to examine the response of high-energy protons (35–70, 70–140, and 140–500 MeV) within $L = 3$ to large geomagnetic storms between 1998 and 2005 inclusive. Their study overlapped with the period analyzed here, and they identified a storm response; however, for the energies in question the proton flux is consistently low at $L = 2.7$, agreeing with the POES observations for the >6.9-MeV proton channel. The difference in orbits between the two satellites could account for some part of this; for example, Fennell et al. (2005) found that electron fluxes were an order of magnitude larger at higher altitudes on the same L-shell, and consequently, the background proton flux at the altitude of POES may be significantly smaller and within the noise of the instrument. It is also important to note that each of the events that have been identified in the >30-keV electron flux is associated with an increase in flux in the precipitating and trapped fluxes, and so the increased ionization seen by the MF radar cannot be caused just by the loss of an existing proton population.

A subset of the slot region filling events were associated with increases in proton flux connected to an SPE. However, several events with an ionospheric counterpart did not have protons present, indicating that energetic electrons are precipitating into the atmosphere above Rothera. For those events associated with large absolute values of SYM-H there is likely to be a mix of electrons and protons that have gained access due to a suppressed geomagnetic cut-off. There is no evidence for the sustained proton background identified by Selesnick et al. (2010) at the orbital altitudes of POES.

4.3. Local Time Variation in Precipitation

The MF radar passes through all local times and as such can be used to probe the variation in precipitation in magnetic local time (MLT). Figure 4 demonstrates that there are local time effects in the ΔSNR due to solar illumination/photochemistry effects in the D region; these need to be removed from the data to see the residual precipitation variation. The average local time response can be determined by removing data when the solar elevation angle is beyond a given threshold at which photochemical effects start to become important. Collis and Rietveld (1991) used incoherent scatter radar measurements to examine changes in electron density over twilight; although there were differences between sunset and sunrise, there was a near-linear relationship between the solar zenith angle (χ) and the decrease/increase in electron density beyond $\chi = 90°$, even though the mesospheric altitudes were illuminated. Therefore, periods have been selected only when $\chi < 90°$ to examine the MLT effect of precipitation.

Figure 9 presents hourly data, binned as a function of MLT. Figures 9a–9c show the median ΔSNR as a function of MLT and day from epoch for three altitude gates: 60.5, 74.5, and 90.5 km. In an attempt to ensure that these plots represent electron precipitation, the data are limited to effective events with maximum solar proton flux <100 cm^{-2}·s^{-1}·sr^{-1} and a minimum SYM-H index >150 nT. This leaves 11 events that contribute to the median ΔSNR; areas shaded in gray are when no data are available, and this is due to the solar zenith angle limit. Each altitude slice shows a response following the zero epoch; ΔSNR is broadly uniform in MLT at each altitude and lasts for 10 days. The data beyond day 10 are somewhat noisier, indicative of some events having a longer duration. At 60.5 km there is a hint of an MLT dependence with the precipitation maximizing between dusk and dawn, but it is small and inconclusive. The lack of data close to midnight (23–01 MLT) means that nothing can be concluded about the precipitation at these times.

To further analyze the MLT variation in altitude, the average of the first 5 days following the epoch is taken; this is presented in Figure 9d1. For comparison the average with no χ limitation is shown in Figure 9d2; this shows a local time effect due to the solar illumination (as described in section 3.2) that agrees with the findings of Collis and Rietveld (1991): Change begins below 80 km with an asymmetry between the sunrise/sunset transitions.

When the $\chi < 90$ limitation is imposed (Figure 9d1), the MLT variation disappears. The transition from positive to negative ΔSNR occurs consistently between 68- and 76-km altitude; some spreading in altitude is expected due to the mixing of events that may contain different energies of precipitating particles. The MLT pattern in ΔSNR appears symmetric about noon and is uniform in the transition region. Above and below the transition, there is an increase in ΔSNR at both high and low altitudes between 07 and 17 MLT. It is important to note that the amount of data contributing to the medium varies from 11 events at noon to 5 at dusk and dawn to 1 at 02 and 22 MLT. This introduces some uncertainty into the measurement, and so caution must be applied in interpreting the MLT pattern. The most likely conclusion is that the change with MLT is a combination of the low number of events coupled with a photoionization effect that is not completely removed by a $\chi < 90$ limit. If the dayside/nightside change was due to a precipitation effect, one should expect ΔSNR to reduce (increase) at higher altitudes as it increases (decreases) at lower (see section 2.2). Similarly, one would expect the height of transition to vary.

Although it is not possible to resolve the full precipitation pattern in MLT, there is enough information available to limit the possible causes of the precipitation. The chief mechanism for the precipitation of particles from the radiation belts is scattering into the loss cone through interaction with electromagnetic waves. Several waves interact with energetic electrons and modify their pitch angles, and the three primary natural candidates are whistler mode chorus, hiss, and electromagnetic ion cyclotron waves (e.g., Thorne, 2010); magnetosonic waves will also modify electron pitch angle distributions though they tend to accelerate electrons and not lead to precipitation. Recent work has suggested that the combined scattering from hiss and

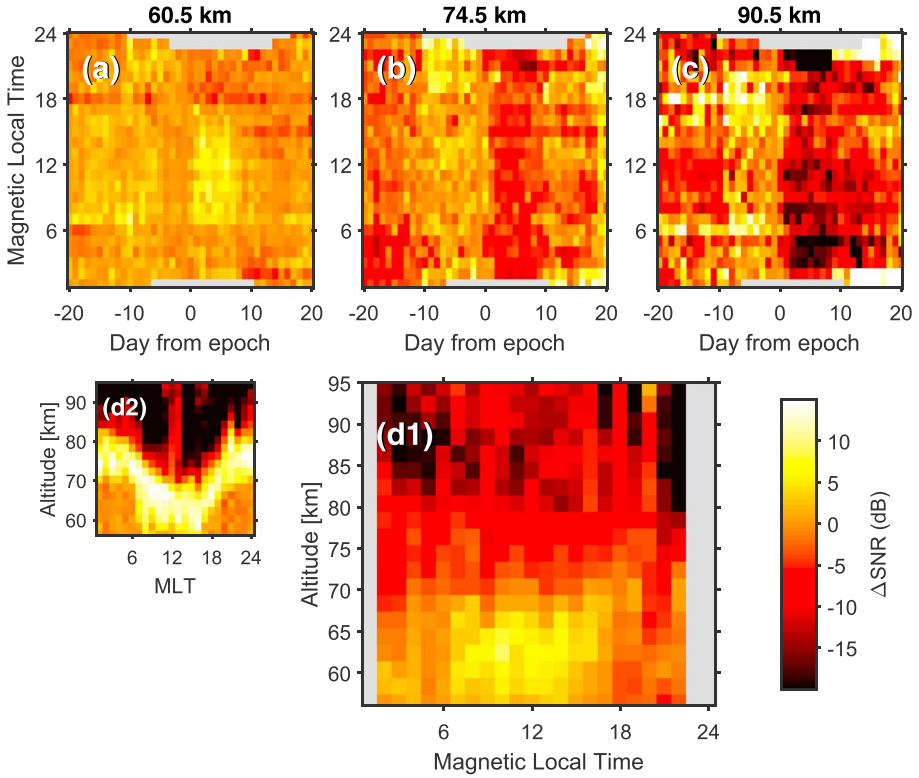

Figure 9. Magnetic local time distribution of change in signal-to-noise ratio (ΔSNR) for those events where $\Delta J_e > 300$ cm^{-2}·s^{-1}·sr^{-1}. Data are in hourly averages and have been restricted to those events with a solar proton flux of <100 cm^{-2}·s^{-1}·sr^{-1} and a minimum SYM-H of -150 nT. The data are further restricted by a solar zenith angle (χ) limit of 90°. Eleven events contribute to the median ΔSNR though this tapers to zero at the edges. The top three panels show ΔSNR (color scale) at three heights for magnetic local time on the *y*-axis and the epoch time on the *x*-axis: (a) at 60.5 km, (b) at 74.5 km, and (c) at 90.5 km. The lower two panels show the average ΔSNR calculated from the 5 days following the onset. (d1) The result with the χ criterion imposed. (d2) The result with no limit on χ, showing the natural variation that masks the precipitation effect.

magnetosonic waves can lead to a slowdown in loss of ~100-keV electrons (Ni et al., 2017) from the magnetosphere such that magnetosonic wave may have a role in the process.

The distributions of waves in the magnetosphere are both MLT and *L*-shell dependent, but at *L* close to the radar site (*L* = 2.7) whistler mode chorus tends to occur from pre-midnight, through dawn to postnoon, and electromagnetic ion cyclotron waves lie from midnight to dusk. These local time variations do not match the MLT pattern of SNR observed by the MF radar. However, considering our comments on the number of data points behind Figure 9 and the caution that must be observed, we cannot completely rule out chorus as a possible factor. It is more likely that hiss is the dominant wave driving the precipitation. Thorne (2010) describes hiss as "an incoherent whistler-mode emission confined within the dense plasmasphere." It has been mooted as the primary cause of the formation of the slot region during quiet times (e.g., Lyons & Thorne, 1973). Meredith et al. (2007) examined the electron *e*-folding loss timescales in the slot region and considered both hiss and lightning-generated whistler mode waves. They found that the timescale for 2-MeV electrons to be lost due to hiss propagating at small wave normal angles at *L* = 2.5 is 1–10 days. This is consistent with the timescale of average precipitation during these slot region filling events. They also showed wave intensities as a function of *L*, MLT, and geomagnetic activity using data from the Combined Release and Radiation Effects Satellite (CRRES) satellite (Anderson et al., 1992). For moderate and active geomagnetic conditions (as measured by the AE* index, where AE* is the maximum value of AE in the previous 3 hr) the average wave intensity is strongest on the dayside at the *L*-shell corresponding to the radar measurements. Thus, the local time distribution of ΔSNR is consistent with plasmaspheric hiss being the principal cause of precipitation. It is worth noting that the pattern of Hiss intensity shown in Figure 1 of Meredith et al. (2007) matches the MLT distribution of ΔSNR very well; however, given the uncertainty attached to the

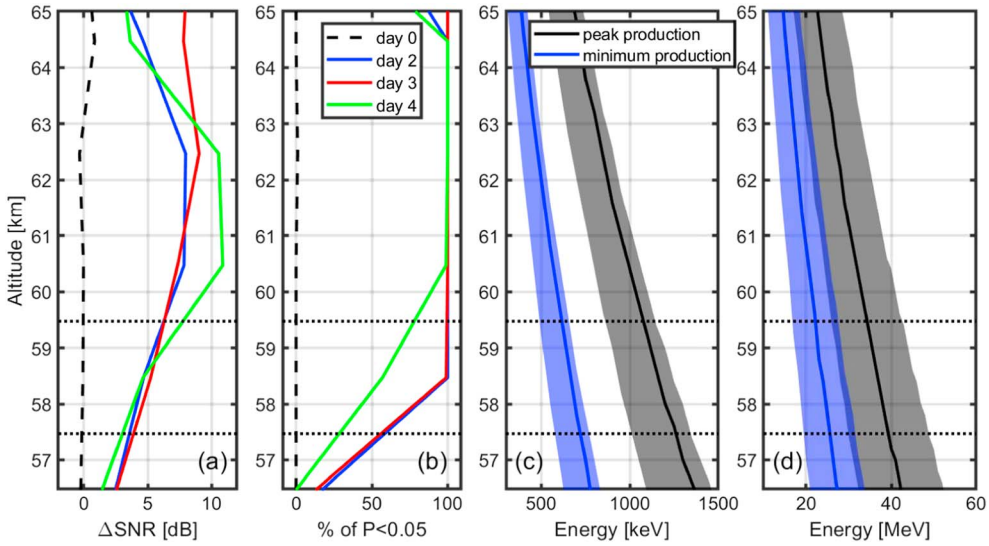

Figure 10. (a) Height profiles of change in signal-to-noise ratio (ΔSNR) for days 0, 2, 3, and 4 of the epoch. (b) The equivalent Kolmogorov-Smirnov test results as described for Figure 7. This value is used to determine at what height the precipitation effect disappears. The minimum height of deposition (blue line) and height of peak ionization (black line) as a function of energy for (c) electrons and (d) protons. The shaded regions indicate the spread of data from all of the events that contribute. The horizontal dotted lines show the boundaries of the range gate centered on 58.5-km altitude.

measurements on the nightside, more data are needed to confirm whether this is more than coincidence. We cannot absolutely rule out chorus, or the influence of magnetosonic waves, though the lack of variability in ΔSNR amplitude would suggest that there is no damping of the interaction (unless it occurs at all MLT) or a change in the scattering process. Given that the MLT distribution of ΔSNR does not show a variation in altitude, it would appear that the precipitation mechanism (whether that be interaction with hiss or something else) is moderately independent of energy.

4.4. Energy Estimates

The altitude profile of the perturbation in the SNR detected by the MF radar provides information on the peak energy of the precipitation. In practice, this is limited by the lowest energy flux that generates ionization that is detectable by the radar, a quantity that is currently unknown. Consequently, an estimate of peak energy from the radar can be considered as the minimum possible value of the peak energy of precipitation; higher energies may be present at low flux levels beyond the ability of the radar to detect them. A key factor in analyzing the radar response is determining the height at which there is confidence that the radar is responding to the precipitation.

Figure 10 shows how the minimum peak energy can be estimated for the average of events with $300 < \Delta J_e < 800$ cm^{-2}·s^{-1}·sr^{-1}; this excludes the largest events. Figure 10a shows the median ΔSNR of the >300 cm^{-2}·s^{-1}·sr^{-1} events below 65-km altitude for the day of the epoch (black dashed lines), day 2 (blue line), day 3 (red line), and day 4 (green line). Day 1 from the epoch was not included as this will contain a mix of preonset and postonset effects depending on the actual universal time of the onset of precipitation and the local time of the radar. The largest perturbation occurred in the 60.5-km (day 4) or 62.5-km (days 2 and 3) range gates, before reducing at lower altitudes. The median ΔSNR does not reach pre-event levels within detectable range. Figure 10b shows the results of the significance tests for the corresponding days. The *x*-axis shows the percentage number of tests where the *p* value was below 0.05. For days 2 to 4 the *p* value was below 0.05 over 90% of the time above 58.5 km, dropping rapidly to zero by the next altitude range gate of the radar (56.5 km). The dotted black lines represent the edges of the 58.5-km range gate at 2 km wide.

A charged particle precipitating through the atmosphere will produce an ionization profile (e.g., Rees, 1963; Semeter & Kamalabadi, 2005) that is primarily dependent on three parameters: the mass of the particle, the density profile of the atmosphere through which the particle travels, and the energy of the precipitating particle. As the particle descends through the atmosphere, the ionization increases, until it peaks at some altitude and rapidly drops to zero. Due to the dependence on the neutral atmosphere

density the profile for a monoenergetic beam of electrons will change depending on the time of year. The magnitude of the ionization profile is dependent on the flux of precipitating particles.

Figures 10c and 10d show energy versus altitude for electrons (Figure 10c) and protons (Figure 10d) hitting the atmosphere. The black line shows the minimum altitudes of penetration (when the ionization drops back to zero), and the blue line shows the altitudes of the peaks of the ionization profiles as a function of energy (*x*-axis). These are the median values calculated for all events in the selected energy range. These curves have been generated using the calculations for ionization rates outlined in Rees (1963). These combine a neutral density profile with an estimate of the range of electrons in air for given energies. The neutral density profile is provided by NRLMSISE-00 (Picone et al., 2002); this introduces a time-of-year effect, and so the shaded regions around each line indicate the spread of values due to this. The range of electrons in a standard atmosphere for electrons and protons have been calculated using data provided by the National Institute of Standards and Technology Physical Measurements Laboratory (https://www.nist.gov/pml/stopping-power-range-tables-electrons-protons-and-helium-ions).

If the MF radar responds to a change in ionization at a given altitude, the corresponding energy on the black line indicates the minimum energy that could cause that ionization. Particles with energy below this threshold will deposit above that altitude and so will not contribute to the ionization. In practice, the drop from the peak to zero point is such that a detectable change in the MF radar SNR is likely to be associated with an energy on the curve between these points.

From Figure 10 it can be seen that for $300 < \Delta J_e < 800$ cm^{-2}·s^{-1}·sr^{-1} the minimum altitude where the radar detected a measurable change in ΔSNR was the 58.5-km range gate. Thus, the minimum peak energy inferred from the height of minimum deposition (blue line in Figure 10c) is 670 ± 50 keV. This rises toward 1170 ± 90 keV when the peak altitude of ionization is considered (black line in Figure 10c). For completeness, protons have been included in Figure 10d, and if this is the dominant source of ionization, then the minimum peak energy lies between 24.2 ± 7.5 and 37.4 ± 11.5 MeV, which would be in line with the observations described by Selesnick et al. (2010). Of the 12 events that made up the selected range, five had no SPEs, two had an SPE with low peak flux (both 24 cm^{-2}·s^{-1}·sr^{-1}), and one with 466 cm^{-2}·s^{-1}·sr^{-1} was accompanied by a minimum SYM-H of −70. Thus, eight out of the 12 were highly unlikely to have high fluxes of protons present such that electrons are likely to have been dominant. The estimated minimum peak value (670–1170 keV) suggests that relativistic energies are present and are in line with the increased precipitating J_p flux being due to contamination.

The superposed epoch analysis technique is a good means of extracting the average behavior, especially when the input data are somewhat noisy, but it masks responses away from the average. The events were selected based upon their integral flux level, and consequently, no spectral information was considered. Consequently, considering the average (whether mean or median) of those events will ignore the potential for more energetic precipitation.

Figure 11 presents two examples of $300 < \Delta J_e < 800$ cm^{-2}·s^{-1}·sr^{-1} events. The two left-hand panels show the SNR from the day prior to precipitation onset (black line) and the day after onset (blue line) for 2 October 2002 (Figure 11a) and 24 August 2005 (Figure 11d). These are analogous to before and after the dashed line at $t = \tau_0$ in Figure 1: Pre-precipitation, the SNR increases with altitude as the electron density increases before reducing again as either the signal is absorbed or the scattering efficiency decreases (black line); with precipitation the increased electron density at low altitudes leads to increased SNR with a drop-off in signal at increasing altitudes as the signal undergoes absorption (blue line). Thus, from the model of the radar response to precipitation, one would expect to see two points of convergence between the lines: The highest altitude point is where the upward trending SNR (quiet day) passes the downward trending SNR (active day). The lowest altitude convergence therefore gives an indication of the lowest altitude limit where an increased electron density can be detected.

The right-hand panels show the corresponding energy deposition heights, where the blue line is the height of peak deposition for a given energy and the red line is the minimum height of deposition for a given energy. These have been calculated for the day after onset in each case. In Figures 11a and 11d the SNR value is the hourly median (at each height) around noon; the error bars are determined from the median absolute

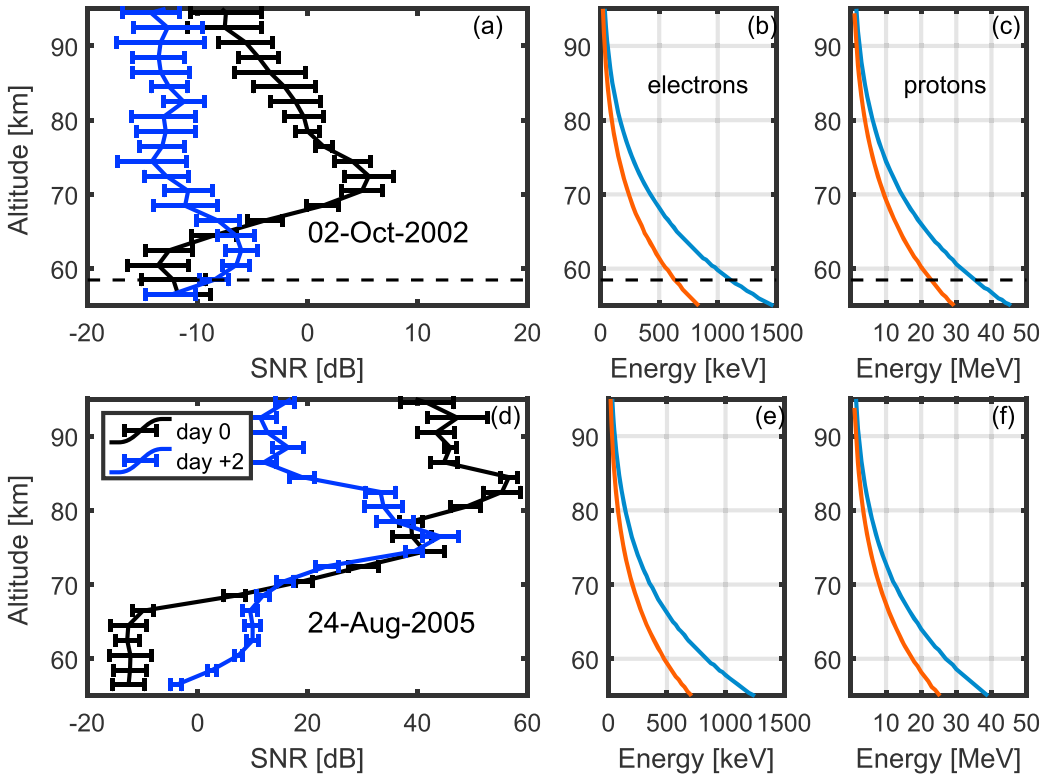

Figure 11. Two example events on 2 October 2002 and 24 August 2005. (a and d) The height profiles of the signal-to-noise ratio (SNR) on the day prior to onset (black) and the day after onset (blue); error bars are derived from the median absolute deviation. (b and e) The minimum height of deposition (red line) and peak altitude of ionization (blue line) for electrons as a function of energy. (c and f) The same for protons. The horizontal dashed line in the top row indicates the center of the lowest radar altitude bin where the SNR converges.

deviation. For each event there is a similar pattern: a reduction in SNR at higher altitudes with an increase at the lower ranges (e.g., as suggested in Figure 1); the height of transition changes between the events, and this is likely due to a number of factors that include the seasonal differences in the background ionosphere and the spectrum of precipitation. In Figure 11a the two profiles converge below the 58.5-km range gate, as shown by the horizontal dashed black line. This corresponds to an energy of 640 ± 50 keV, perhaps as high as 1,120 ± 90 keV. In Figure 11d the profiles do not converge within the radar height range, suggesting that for this event the electron are penetrating deep into the lower mesosphere below 54.5-km altitude (the bottom of the lowest range gate). The bottom of the radar range corresponds to 630 ± 50 keV with an 1,110 ± 80 keV peak deposition.

The proton curves have been added for completeness (Figures 11c and 11f); the 24 August 2005 event was accompanied by a modest SPE that peaked on the day prior to the flux increase (max flux = 330 $cm^{-2}{\cdot}s^{-1}{\cdot}sr^{-1}$). The minimum SYM-H value was −174 nT, which is not particularly strong but means that an injection of energetic protons cannot be ruled out. If protons are responsible, this would be between 25 and 40 MeV. For 2 October 2002 there was no SPE during this event such that the corresponding increase in J_e for both the trapped and precipitating detectors could not be due to an influx of protons. Although this was in the period where Selesnick et al. (2010) noted an extant proton population, this cannot explain the apparent increase in both trapped and precipitating electron fluxes. The event did record an increase in the trapped and precipitating J_p; this is indicative of contamination by energetic electrons (upward of 700 keV).

The uncertainties in this technique arise from several sources. Semeter and Kamalabadi (2005) provide a good discussion of the inputs to the ionization calculation. For example, the final ionization curve depends on the assumed pitch angle distribution of incident electrons; for lower-energy electrons (few keV) the isotropic distribution has been found to better reflect reality (e.g., Semeter et al., 2001). Given that higher-energy

electrons tend toward isotropic, this is the distribution we adopt. Uncertainties will always arise due to the choice of atmospheric density profile, but in the absence of direct measurements NRLMSISE-00 is the best option. Finally, the greatest uncertainty in the estimate is where to on the ionization curve the bottom edge of the change in ΔSNR corresponds. Is it closer to the peak of ionization or to the point where the ionization curve drops to zero? In the absence of a means of answering this question we must present a range of energies to represent the minimum peak energy of precipitation.

Thus, in combination with an ionization profile model the MF radar at Rothera can provide a minimum estimate of the most energetic electrons precipitating from the slot region. This technique provides a ground truth to confirm the observations from the POES that during these events, when the slot region is filled by >30 keV electrons, there is a steady loss to the atmosphere that lasts an average of 10 days. Although the MF radar cannot discriminate between the sources of additional ionization it is important to note that it provides a clear indicator of precipitation occurring down to the stratopause. This precipitation does not appear to be confined in MLT and can occur during moderate geomagnetic activity.

When considering the atmospheric response to charged particle precipitation, it is important to ensure that the slot region is included as a source. This is particularly true in the Southern Hemisphere with the large separation of the geographic and geomagnetic poles. Rothera, located on the Antarctic Peninsula, is at a relatively high geographic latitude while being at quite a low geomagnetic latitude. During winter months it is usually within the stable southern polar vortex. The precipitation from the slot region, whether it be electron or proton, is depositing energy close to the stratopause, generating NO_x that can be transported further downward to where ozone is more abundant. Further analyis is required to determine the impact of these events.

5. Conclusions

Between 2002 and 2014 inclusive, the POES satellites detected 54 instances when the radiation belt slot region was filled for more than 1 day by fluxes of electrons with energy in excess of 30 keV. Of these events, 20 were also detected by an MF radar located at Rothera in Antarctica at $L = 2.7$. The radar observed a change in the SNR during these events caused by changes in the local ionization due to the precipitation of charged particles. An analysis of these events leads to the following conclusions:

1. Significant energetic precipitation into the ionosphere occurs from the slot region at times when it is filled. The duration of precipitation is ~10 days on average.
2. Slot region filling events are not uncommon, and consequently, geomagnetic storms have a larger area of precipitation than just the auroral zones and outer radiation belts. Thus, atmospheric models that include energetic precipitation must include the slot region.
3. There is a weak dependence on geomagnetic storm strength (as indicated by SYM-H); however, a large number (18 out of 49) of slot region filling events occur for moderate activity (minimum SYM-H > -100 nT).
4. The precipitation is energetic, penetrating into the lower mesosphere, potentially to the stratopause (50- to 55-km altitude).
5. In some cases there is a mixture of high-energy electrons and protons; however, for some events electrons are likely to be the dominant species. The height of deposition suggests that these electrons are in excess of 640 keV, perhaps higher than 1 MeV.
6. The distribution of the precipitation in MLT is consistent with scattering by plasmaspheric hiss.

The MF radar can provide a ground truth to indicate times when energetic precipitation is occurring and can provide bounds on the peak energy of precipitation, when used in conjunction with an atmospheric ionization model.

Acknowledgments
The Rothera MF radar is a joint project between the British Antarctic Survey and GATS Inc., Boulder, USA. Work on the MF radar at BAS is supported via NERC (NE/R016038/1) and was partially supported by NERC grant NE/I010173/1. Data from the MF radar are available from the UK Polar Data Centre (https://www.bas.ac.uk/data/uk-pdc/). We would like to thank all of the staff who have wintered at Rothera station and in particular the electronics engineers who have been responsible for maintaining the MF radar. POES data were obtained from www.spaceweather.ac.uk, which was developed as part of the EU SPACECAST project and is maintained by the Polar Data Centre. We acknowledge the NOAA National Geophysical Data Center, now called the National Centers for Environmental Information, for the original provision of the POES SEM data, and thank all of the scientists, particularly Janet Green, who have worked hard to improve this data set. We acknowledge use of NASA/GSFC's Space Physics Data Facility's OMNIWeb service, and OMNI data and the World Data Center for Geomagnetism, Kyoto, for the SYM-H data. We would like to thank Mervyn Freeman for useful conversations when conducting this research.

References

Anderson, R. R., Gurnett, D. A., & Odem, D. L. (1992). CRRES plasma wave experiment. *Journal of Spacecraft and Rockets*, *29*(4), 570–573. https://doi.org/10.2514/3.25501

Baker, D. N., Kanekal, S. G., Hoxie, V. C., Henderson, M. G., Li, X., Spence, H. E., et al. (2013). A long-lived relativistic electron storage ring embedded in Earth's outer Van Allen belt. *Science*, *340*(6129), 186–190. https://doi.org/10.1126/science.1233518

Baker, D. N., Kanekal, S. G., Li, X., Monk, S. P., Goldstein, J., & Burch, J. L. (2004). An extreme distortion of the Van Allen belt arising from the Halloween solar storm in 2003. *Nature*, *432*(7019), 878–881. https://doi.org/10.1038/nature03116

Briggs, B. H. (1984). The analysis of spaced sensor records by correlation techniques. In *Handbook for MAP* (Vol. 13, pp. 166–186). Urbana: SCOSTEP Secr., Univ. of Ill.

Califf, S., Li, X., Zhao, H., Kellerman, A., Sarris, T. E., Jaynes, A., & Malaspina, D. M. (2017). The role of the convection electric field in filling the slot region between the inner and outer radiation belts. *Journal of Geophysical Research: Space Physics*, *122*, 2051–2068. https://doi.org/10.1002/2016JA023657

Collis, P. N., & Rietveld, M. T. (1991). Mesospheric observations with the EISCAT UHF radar during polar cap absorption events: 1. Electron densities and negative ions. *Annales de Geophysique*, *8*, 809–824.

Davies, K. (1990). *Ionospheric Radio*, London, UK: Peter Peregrinus Ltd on behalf of the IEE.

Evans, D., Garrett, H., Jun, I., Evans, R., & Chow, J. (2008). Long-term observations of the trapped high-energy proton population (L < 4) by the NOAA Polar Orbiting Environmental Satellites (POES). *Advances in Space Research*, *41*(8), 1261–1268. https://doi.org/10.1016/j.asr.2007.11.028

Evans, D. S., & Greer, M. S. (2004). Polar orbiting environmental satellite space environment monitor-2 instrument descriptions and archive data documentation, NOAA Tech. Mem. 1.4, Space Environ. Lab., Boulder, CO.

Fennell, J. F., Blake, J. B., Friedel, R., & Kanekal, S. (2005). The energetic electron response to magnetic storms: HEO satellite observations. In *Physics and modeling of the inner magnetosphere*, *AGU monograph* (Vol. 155, pp. 87–95). Washington DC: American Geophysical Union.

Ganushkina, N. Y., Pulkkinen, T. I., Sergeev, V. A., Kubyshkina, M. V., Baker, D. N., Turner, N. E., et al. (2000). Entry of plasma sheet particles into the inner magnetosphere as observed by Polar/CAMMICE. *Journal of Geophysical Research*, *105*(A11), 25,205–25,219. https://doi.org/10.1029/2000JA900062

Gardner, F. F., & Pawsey, J. L. (1953). Study of the ionospheric D-region using partial reflections. *Journal of Atmospheric and Terrestrial Physics*, *3*, 321–344.

Horne, R. B., Meredith, N. P., Glauert, S. A., Varotsou, A., Boscher, D., Thorne, R. M., et al. (2006). Mechanisms for the acceleration of radiation belt electrons. In B. T. Tsurutani, et al. (Eds.), *Co-rotating solar wind streams and recurrent geomagnetic activity*, *Geophysical Monograph Series* (Vol. 167, pp. 151–173). Washington, DC: American Geophysical Union.

Kavanagh, A. J., Marple, S. R., Honary, F., McCrea, I. W., & Senior, A. (2004). On solar protons and polar cap absorption: Constraints on an empirical relationship. *Annales de Geophysique*, *22*(4), 1133–1147.

Kolmogorov, A. (1933). Sulla determinazione empirica di una legge di distribuzione. *Giornale dell'Istituto Italiano degli Attuari*, *4*, 83–91.

Kress, B. K., Hudson, M. K., Perry, K. L., & Slocum, P. L. (2004). Dynamic modeling of geomagnetic cutoff for the 23–24 November 2001 solar energetic particle event. *Geophysical Research Letters*, *31*, L04808. https://doi.org/10.1029/2003GL018599

Lam, M. M., Horne, R. B., Meredith, N. P., Glauert, S. A., Moffat-Griffin, T., & Green, J. C. (2010). Origin of energetic electron precipitation >30 keV into the atmosphere. *Journal of Geophysical Research*, *115*, A00F08. https://doi.org/10.1029/2009JA014619

Li, W., Ma, Q., Thorne, R. M., Bortnik, J., Kletzing, C. A., Kurth, W. S., et al. (2015). Statistical properties of plasmaspheric hiss derived from Van Allen probes data and their effects on radiation belt electron dynamics. *Journal of Geophysical Research: Space Physics*, *120*, 3393–3405. https://doi.org/10.1002/2015JA021048

Li, X., Baker, D. N., Temerin, M., Cayton, T. E., Reeves, G. D., Christensen, R. A., et al. (1997). Multi-satellite observations of the outer zone electron variation during the November 3–4, 1993, magnetic storm. *Journal of Geophysical Research*, *102*(A7), 14,123–14,140. https://doi.org/10.1029/97JA01101

Liu, S., Chen, M. W., Lyons, L. R., Korth, H., Albert, J. M., Roeder, J. L., et al. (2003). Contribution of convective transport to stormtime ring current electron injection. *Journal of Geophysical Research*, *108*(A10), 1372. https://doi.org/10.1029/2003JA010004

Lorentzen, K. R., Mazur, J. E., Looper, M. D., Fennell, J. F., & Blake, J. B. (2002). Multisatellite observations of MeV ion injections during storms. *Journal of Geophysical Research*, *107*(A9), 1231. https://doi.org/10.1029/2001JA000276

Loto'aniu, T. M., Mann, I. R., Ozeke, L. G., Chan, A. A., Dent, Z. C., & Milling, D. K. (2006). Radial diffusion of relativistic electrons into the radiation belt slot region during the 2003 Halloween geomagnetic storms. *Journal of Geophysical Research*, *111*, A04218. https://doi.org/10.1029/2005JA011355

Lyons, L. R., & Thorne, R. M. (1973). Equilibrium structure of radiation belt electrons. *Journal of Geophysical Research*, *78*(13), 2142–2149. https://doi.org/10.1029/JA078i013p02142

Mann, I. R., Ozeke, L. G., Murphy, K. R., Claudepierre, S. G., Turner, D. L., Baker, D. N., et al. (2016). Explaining the dynamics of the ultra-relativistic third Van Allen radiation belt. *Nature Physics*, *12*(10), 978–983. https://doi.org/10.1038/nphys3799

Mann, I. R., Ozeke, L. G., Murphy, K. R., Claudepierre, S. G., Turner, D. L., Baker, D. N., et al. (2018). Reply to 'The dynamics of Van Allen belts revisited'. *Nature Physics*, *14*(2), 103–104. https://doi.org/10.1038/nphys4351

Meredith, N. P., Horne, R. B., Glauert, S. A., & Anderson, R. R. (2007). Slot region electron loss timescales due to plasmaspheric hiss and lightning-generated whistlers. *Journal of Geophysical Research*, *112*, A08214. https://doi.org/10.1029/2007JA012413

Meredith, N. P., Horne, R. B., Glauert, S. A., Baker, D. N., Kanekal, S. G., & Albert, J. M. (2009). Relativistic electron loss timescales in the slot region. *Journal of Geophysical Research*, *114*, A03222. https://doi.org/10.1029/2008JA013889

Ni, B., Bortnik, J., Thorne, R. M., Ma, Q., & Chen, L. (2013). Resonant scattering and resultant pitch angle evolution of relativistic electrons by plasmaspheric hiss. *Journal of Geophysical Research: Space Physics*, *118*, 7740–7751. https://doi.org/10.1002/2013JA019260

Ni, B., Cao, X., Zou, Z., Zhou, C., Gu, X., Bortnik, J., et al. (2015). Resonant scattering of outer zone relativistic electrons by multi-band EMIC waves and resultant electron loss timescales. *Journal of Geophysical Research: Space Physics*, *120*, 7357–7373. https://doi.org/10.1002/2015JA021466

Ni, B., Hua, M., Zhou, R., Yi, J., & Fu, S. (2017). Competition between outer zone electron scattering by plasmaspheric hiss and magnetosonic waves. *Geophysical Research Letters*, *44*, 3465–3474. https://doi.org/10.1002/2017GL072989

Ni, B., Xiang, Z., Gu, X., Shprits, Y. Y., Zhou, C., Zhao, Z., et al. (2016). Dynamic responses of the Earth's radiation belts during periods of solar wind dynamic pressure pulse based on normalized superposed epoch analysis. *Journal of Geophysical Research: Space Physics*, *121*, 8523–8536. https://doi.org/10.1002/2016JA023067

Park, J., Min, K. W., Summers, D., Hwang, J., Kim, H. J., Horne, R. B., et al. (2010). Non-stormtime injection of energetic particles into the slot-region between Earth's inner and outer electron radiation belts as observed by STSAT-1 and NOAA-POES. *Geophysical Research Letters*, *37*, L16102. https://doi.org/10.1029/2010GL043989

Picone, J. M., Hedin, A. E., Drob, D. P., & Aikin, A. C. (2002). NRLMSISE-00 empirical model of the atmosphere: Statistical comparisons and scientific issues. *Journal of Geophysical Research*, *107*(A12), 1468. https://doi.org/10.1029/2002JA009430

Rees, M. H. (1963). Auroral ionization and excitation by incident energetic electrons. *Planetary and Space Science*, *11*(10), 1209–1218. https://doi.org/10.1016/0032-0633(63)90252-6

Reeves, G. D., Friedel, R. H. W., Belian, R. D., Meier, M. M., Henderson, M. G., Onsager, T., et al. (1998). The relativistic electron response at geosynchronous orbit during the January 1997 magnetic storm. *Journal of Geophysical Research*, *103*(A8), 17,559–17,570. https://doi.org/10.1029/97JA03236

Reid, G. C. (1974). Polar-cap absorption—Observations and theory. *Fundamentals of Cosmic Physics*, *1*(3), 167–200.
Rietveld, M. T., & Collis, P. N. (1993). Mesospheric observations with the EISCAT UHF radar during polar cap absorption events: 2. Spectral measurements. *Annales de Geophysique*, *11*, 797–808.
Rodger, C. J., Clilverd, M. A., Green, J. C., & Lam, M. M. (2010). Use of POES SEM-2 observations to examine radiation belt dynamics and energetic electron precipitation into the atmosphere. *Journal of Geophysical Research*, *115*, A04202. https://doi.org/10.1029/2008JA014023
Rodger, C. J., Clilverd, M. A., Verronen, P. T., Ulich, T., Jarvis, M. J., & Turunen, E. (2006). Dynamic geomagnetic rigidity cutoff variations during a solar proton event. *Journal of Geophysical Research*, *111*, A04222. https://doi.org/10.1029/2005JA011395
Rodger, C. J., Kavanagh, A. J., Clilverd, M. A., & Marple, S. R. (2013). Comparison between POES energetic electron precipitation observations and riometer absorptions: Implications for determining true precipitation fluxes. *Journal of Geophysical Research: Space Physics*, *118*, 7810–7821. https://doi.org/10.1002/2013JA019439
Rusch, D. W., Gerard, J.-C., Solomon, S., Crutzen, P. J., & Reid, G. C. (1981). The effect of particle precipitation events on the neutral and ion chemistry of the middle atmosphere-I. Odd nitrogen. *Planetary and Space Science*, *29*(7), 767–774. https://doi.org/10.1016/0032-0633(81)90048-9
Selesnick, R. S., Hudson, M. K., & Kress, B. T. (2010). Injection and loss of inner radiation belt protons during solar proton events and magnetic storms. *Journal of Geophysical Research*, *115*, A08211. https://doi.org/10.1029/2010JA015247
Semeter, J., & Kamalabadi, F. (2005). Determination of primary electron spectra from incoherent scatter radar measurements of the auroral E region. *Radio Science*, *40*, RS2006. https://doi.org/10.1029/2004RS003042
Semeter, J., Vogt, J., Haerendel, G., Lynch, K., & Arnoldy, R. (2001). Persistent quasiperiodic precipitation of suprathermal ambient electrons in decaying auroral arcs. *Journal of Geophysical Research*, *106*(A7), 12,863–12,873. https://doi.org/10.1029/2000JA000136
Seppälä, A., Clilverd, M. A., & Rodger, C. J. (2007). NO_x enhancements in the middle atmosphere during 2003–2004 polar winter: Relative significance of solar proton events and the aurora as a source. *Journal of Geophysical Research*, *112*, D23303. https://doi.org/10.1029/2006JD008326
Seppälä, A., Lu, H., Clilverd, M. A., & Rodger, C. J. (2013). Geomagnetic activity signatures in wintertime stratosphere wind, temperature, and wave response. *Journal of Geophysical Research: Atmospheres*, *118*, 2169–2183. https://doi.org/10.1002/jgrd.50236
Seppälä, A., Randall, C. E., Clilverd, M. A., Rozanov, E., & Rodger, C. J. (2009). Geomagnetic activity and polar surface air temperature variability. *Journal of Geophysical Research*, *114*, A10312. https://doi.org/10.1029/2008JA014029
Seppälä, A., Verronen, P. T., Clilverd, M. A., Randall, C. E., Tamminen, J., Sofieva, V., et al. (2007). Arctic and Antarctic polar winter NO_x and energetic particle precipitation in 2002–2006. *Geophysical Research Letters*, *34*, L12810. https://doi.org/10.1029/2007GL029733
Shprits, Y. Y., Horne, R. B., Kellerman, A. C., & Drozdov, A. Y. (2018). The dynamics of the Van Allen belts revisited. *Nature Physics*, *14*(2), 102–103. https://doi.org/10.1038/nphys4350
Shprits, Y. Y., Thorne, R. M., Horne, R. B., Glauert, S. A., Cartwright, M., Russell, C. T., et al. (2006). Acceleration mechanism responsible for the formation of the new radiation belt during the 2003 Halloween solar storm. *Geophysical Research Letters*, *33*, L05104. https://doi.org/10.1029/2005GL024256
Siskind, D. E., Nedoluha, G. E., Randall, C. E., Fromm, M., & Russell, J. M. (2000). An assessment of Southern Hemisphere stratospheric NO_x enhancements due to transport from the upper atmosphere. *Geophysical Research Letters*, *27*(3), 329–332. https://doi.org/10.1029/1999GL010940
Smirnov, N. (1948). Table for estimating the goodness of fit of empirical distributions. *Annals of Mathematical Statistics*, *19*(2), 279–281. https://doi.org/10.1214/aoms/1177730256
Solomon, S., Rusch, D. W., Gerard, J.-C., Reid, G. C., & Crutzen, P. J. (1981). The effect of particle precipitation events on the neutral and ion chemistry of the middle atmosphere: II. Odd hydrogen. *Planetary and Space Science*, *8*, 885–893.
Sugiura, M., & Poros, D. J. (1971). Hourly values of equatorial Dst for years 1957 to 1970, Rep. X-645-71-278. Greenbelt, MD Goddard Space Flight Center.
Thorne, R. M. (2010). Radiation belt dynamics: The importance of wave-particle interactions. *Geophysical Research Letters*, *37*, L22107. https://doi.org/10.1029/2010GL044990
Thorne, R. M., Horne, R. B., Glauert, S. A., Meredith, N. P., Shprits, Y. Y., Summers, D., et al. (2005). The influence of wave-particle interactions on relativistic electrons during storms. In J. Burch, M. Schulz, & H. Spence (Eds.), *Inner magnetosphere interactions: New perspectives from imaging*, *Geophysical Monograph Series* (Vol. 159, pp. 101–112). Washington, DC: American Geophysical Union.
Thrane, E. V., Haug, A., Bjelland, B., Anastassiades, M., & Tsagakis, E. (1968). Measurements of D-region electron densities during the International Quiet Sun years. *Journal of Atmospheric and Terrestrial Physics*, *30*(1), 135–150. https://doi.org/10.1016/0021-9169(68)90047-0
Turunen, E., Verronen, P. T., Seppälä, A., Rodger, C. J., Clilverd, M. A., Tamminen, J., et al. (2009). Impact of different precipitation energies on NO_x generation during geomagnetic storms. *Journal of Atmospheric and Solar–Terrestrial Physics*, *71*(10-11), 1176–1189. https://doi.org/10.1016/j.jastp.2008.07.005
Van Allen, J. A. (1959). The geomagnetically trapped corpuscular radiation. *Journal of Geophysical Research*, *64*(11), 1683–1689. https://doi.org/10.1029/JZ064i011p01683
Yando, K., Millan, R. M., Green, J. C., & Evans, D. S. (2011). A Monte Carlo simulation of the NOAA POES Medium Energy Proton and Electron Detector instrument. *Journal of Geophysical Research*, *116*, A10231. https://doi.org/10.1029/2011JA016671
Zou, H., Zong, Q. G., Parks, G. K., Pu, Z. Y., Chen, H. F., & Xie, L. (2011). Response of high-energy protons of the inner radiation belt to large magnetic storms. *Journal of Geophysical Research*, *116*, A10229. https://doi.org/10.1029/2011JA016733